Systems/Circuits

Synaptic Mechanisms Underlying Temporally Precise Information Processing in the VNLL, an Auditory Brainstem Nucleus

Nikolaos Kladisios,[1] Linda Fischer,[1] Florian Jenzen,[1] Michael Rebhan,[2] ⬤Christian Leibold,[2,3] and Felix Felmy[1]

[1]Institute of Zoology, University of Veterinary Medicine Hannover Foundation, 30559, Hannover, Germany, [2]Department Biology II, Ludwig-Maximilians-University Munich, 82152, Planegg-Martinsried, Germany, and [3]Fakultät für Biologie & Bernstein Center Freiburg, Albert-Ludwigs-Universität Freiburg, 79104, Freiburg im Breisgau, Germany

Large glutamatergic, somatic synapses mediate temporally precise information transfer. In the ventral nucleus of the lateral lemniscus, an auditory brainstem nucleus, the signal of an excitatory large somatic synapse is sign inverted to generate rapid feedforward inhibition with high temporal acuity at sound onsets, a mechanism involved in the suppression of spurious frequency information. The mechanisms of the synaptically driven input–output functions in the ventral nucleus of the lateral lemniscus are not fully resolved. Here, we show in Mongolian gerbils of both sexes that, for stimulation frequencies up to 200 Hz, the EPSC kinetics together with short-term plasticity allow for faithful transmission with only a small increase in latency. Glutamatergic currents are exclusively mediated by AMPARs and NMDARs. Short-term plasticity is frequency-dependent and composed of an initial facilitation followed by depression. Physiologically relevant output generation is limited by the decrease in synaptic conductance through short-term plasticity (STP). At this endbulb synapse, STP acts as a low pass filter and increases the dynamic range of the conductance dependent input–output relation, while NMDAR signaling slightly increases the sensitivity of the input–output function. Our computational model shows that STP-mediated filtering limits the intensity dependence of the spike output, thus maintaining selectivity to sound transients. Our results highlight the interaction of cellular features that together give rise to the computations in the circuit.

Key words: auditory system; endbulb synapse; glutamatergic signaling; synaptic transmission; temporal precision; ventral nucleus of the lateral lemniscus

---

Significance Statement

Auditory information processing in the brainstem is a prerequisite for generating our auditory representation of the environment. Thereby, many processing steps rely on temporally precise filtering. Precise feedforward inhibition is a key motif in auditory brainstem processing and produced through sign inversion at several large somatic excitatory synapses. A particular feature of the ventral nucleus of the lateral lemniscus is to produce temporally precise onset inhibition with little temporal variance independent of sound intensity. Our cell-physiology and modeling data explain how the synaptic characteristics of different current components and their short-term plasticity are tuned to establish sound intensity-invariant onset inhibition that is crucial for filtering out spurious frequency information.

Introduction

The ventral nucleus of the lateral lemniscus (VNLL) is involved in suppressing spurious frequencies, as they occur during

spectral splatter (Spencer et al., 2015), a function based on the octopus cell area (VNLL) inferior colliculus circuitry. Neurons in the ventral aspect of the VNLL receive large, somatic, glutamatergic synapses (Adams, 1997; Berger et al., 2014; Caspari et al., 2015) that originate in the octopus cell region of the cochlear nucleus (Stotler, 1953; Friauf and Ostwald, 1988; Adams, 1997; Schofield and Cant, 1997; Smith et al., 2005) and send GABA-/glycinergic projections to the inferior colliculus (Saint Marie et al., 1997; Kelly et al., 2009; Moore and Trussell, 2017). Thus, VNLL neurons are considered to generate rapid feedforward inhibition. Feedforward inhibition with high temporal precision has been shown to be important not only in the binaural system (Pecka et al., 2008; Myoga et al., 2014; Beiderbeck et al., 2018;

Franken et al., 2021), but also, for example, to enable high-frequency oscillations in the hippocampus (Bartos et al., 2002) and controlling feedforward versus feedback processing in cortico-thalamic loops (Cruikshank et al., 2010). Thereby, the functions differ from rapid subthreshold integration to the generation of oscillatory network behaviors and gating of information.

The physiological hallmark of VNLL neurons with presumably large endbulb synapses is a rapid, temporally accurate onset response, of which the latency is little affected by sound intensity (Covey and Casseday, 1991; Zhang and Kelly, 2006a,b; Liu et al., 2014; Recio-Spinoso and Joris, 2014). Their modulation transfer functions are tuned for onset responses to envelope sounds in a frequency range <250 Hz (Zhang and Kelly, 2006a; Recio-Spinoso and Joris, 2014). Biophysically, ventral VNLL neurons are characterized by an onset action potential (Wu, 1999; Caspari et al., 2015; Franzen et al., 2015; Baumann and Koch, 2017; Kladisios et al., 2020), and membrane dynamics that amplify output frequencies ~20 Hz (Fischer et al., 2018). The endbulb inputs are large, fast, and depress during ongoing activity (Wu, 1999; Caspari et al., 2015; Baumann and Koch, 2017; Kladisios et al., 2020).

In the mature auditory brainstem, NMDAR signaling influences synaptic information transfer and sound processing by its electrogenic component (Kelly and Kidd, 2000; Pliss et al., 2009; Porres et al., 2011; Ammer et al., 2012; Siveke et al., 2018, 2019) . Since NMDAR currents are small in mature auditory brainstem neurons, a small and slow inward current can functionally partake in sound processing. In some auditory synapses, AMPAR currents decay biexponentially with a large, fast and a small, slow component (Berger et al., 2014). Whether this small, slow AMPAR-current component contributes to sound processing is unclear.

Short-term plasticity (STP) is implicated in neuronal filtering (Fortune and Rose, 2001; Chung et al., 2002), gain control (Rothman et al., 2009; Pedroarena, 2020), and temporal integration (Kuba et al., 2002; Cook et al., 2003). STP, and predominantly depression, occurs *in vitro* in nearly all auditory synapses (Friauf et al., 2015). However, in mature mammals, the influence of STP in auditory brainstem structures is debated because *in vitro* observations were not corroborated *in vivo* (Lorteije et al., 2009; Kuenzel et al., 2011). Arguments for solving this contradiction are that *in vivo* release probabilities are very low, so depression is not prominent (Borst, 2010), and the presence of spontaneous activity (Bajo et al., 1998; Hermann et al., 2007; Kopp-Scheinpflug et al., 2008) might put the synapse in an ongoing steady-state depression, resulting in a largely invariant level of input size.

Here, we investigated the synaptic contributions to the generation of output and its temporal precision at the mature endbulb synapse in the VNLL under physiologically relevant conditions. NMDAR, but not slow AMPAR, current components amplify the supra-threshold output and increase the sensitivity of the STP-modulated conductance and frequency-dependent filter functions. Modeling acoustically driven VNLL spiking activity indicates that the presence of STP maintains the specificity of the VNLL output to sound onset and supports invariance of output generation to sound intensities.

Materials and Methods

Animals and ethics statement. Mongolian gerbils (*Meriones unguiculatus*) were bred in the institute's animal facility on a Charles River hereditary background. Animals were kept in a 12 h dark-light cycle at 22°C and 35%-44% humidity and had access to food pellets and water *ad libitum*. Animals of either sex and with an average postnatal age (P) of 25.76 ± 0.5 d (range P18-P37) were used. All experiments were performed in accordance with institutional guidelines and regional laws, and approved by the University's animal welfare committee under TiHo-T-2021-4.

Slice preparation. Animals were anesthetized with isoflurane and decapitated. Brains were rapidly removed in cold preparation solution consisting of the following (in mM): 120 sucrose, 25 NaCl, 25 NaHCO$_3$, 1.25 NaH$_2$PO$_4$, 2.5 KCl, 25 glucose, 0.4 L-ascorbic acid, 3 myo-insitol, 2 Na-pyruvate, 3 MgCl$_2$, and 0.1 CaCl$_2$, with a pH of 7.4 when oxygenated with 95% O$_2$ and 5% CO$_2$. Trimmed brain tissue was cut into 200-µm-thick coronal sections containing the VNLL with a VT1200S vibratome (Leica Microsystems). Slices were incubated at 34°C for 45 min in recording solution containing the following (in mM): 125 NaCl, 25 NaHCO$_3$, 1.25 NaH$_2$PO$_4$, 2.5 KCl, 25 glucose, 0.4 L-ascorbic acid, 3 myo-inositol, 2 Na-pyruvate, 1 MgCl$_2$, and either 2 CaCl$_2$ for voltage-clamp experiments presented in Figure 1, or 1.2 CaCl$_2$ for the remaining data, and with a final pH solution of 7.4 when oxygenated with 95% O$_2$ and 5% CO$_2$.

Slice recordings. Slices were transferred to a recording chamber integrated into an upright microscope (BX51 WI, Olympus) and continuously perfused with recording solution at 33-35°C. Electrophysiological recordings were performed using an EPC10/2 USB amplifier (HEKA) controlled by PatchMaster software. For conductance clamp recordings (see Figs. 3-9), we adapted the system introduced by Yang et al. (2015), where a slave computer was connected via a DA board interface (BNC-2090A, National Instruments) with the HEKA amplifier. The slave computer calculated in near real-time the required stimulation current to accommodate the electrochemical driving force, dictated by the conductance of the appointed templates in relation to the membrane potential of the neuron and reversal potential of the conducting ions. VNLL neurons were visualized by either a TILL-Imago VGA or SCMS PCO.edge 3.1m camera controlled by TILLvisION imaging system (FEI) or Camware64 imaging (PCO Imaging) system, respectively. All reported potentials were corrected for liquid junction potential (LJP) according to Barry (1994), by comparing ionic concentration gradients between intracellular and extracellular solutions (Ammer et al., 2015). The intracellular solution for voltage-clamp experiments contained the following (in mM): 130 Cs-gluconate, 10 HEPES, 20 TEA-Cl, 4 MgATP, 0.3 Na$_2$GTP, 5 Na$_2$-phosphocreatine, 5 Cs-EGTA, 5 Qx-314, and 0.1 spermine, with a calculated LJP of 13.3 mV. For conductance clamp recordings, the internal solution contained the following (in mM): 145 K-gluconate, 15 HEPES, 4.5 KCl, 7 Na$_2$-phosphocreatine, 2 Mg-ATP, 2 K$_2$-ATP, 0.3 Na$_2$GTP, and 0.5 K-EGTA, resulting in an LJP of 15.95 mV. Both solutions also contained 50 µM Alexa-594 for cell visualization. For voltage-clamp experiments, VNLL neurons were held at −63 mV. Access resistance was compensated to a residual of 3 MΩ. For conductance clamp recordings, LJP was corrected online and the bridge balance was set to 100%. Overall, data acquisition rate was set at 50 kHz and filtered with a low-pass cutoff of 3 kHz.

Synaptic currents were evoked with a local monopolar glass electrode filled with recording solution, positioned near a patched neuron. Biphasic synaptic stimulations of 200 µs length were triggered via a stimulator unit (Model 2100 A.M. Systems) and amplified by the EPC10/2. EPSCs were pharmacologically isolated by blocking inhibitory GABA- and glycinergic inputs with 10 µM SR95531 and 1 µM strychnine (Stry), respectively. To isolate different glutamatergic components of the synaptic currents, 10 µM (R)-CPP, 50 µM GYKI-53655, and 20 µM DNQX were applied to, respectively, block NMDAR-, AMPAR- and KAR- (other non-NMDA) mediated currents. To estimate I–V relationships (see Fig. 1), neurons were held from −93 to 67 mV, in 10 mV step intervals and recorded in 2 mM extracellular Ca^{2+} concentration. As pharmacologically verified, the EPSC peak at the stimulus onset was defined as the AMPAR, and the residual current 5 ms afterward as the NMDAR current. The decay time of synaptic inputs was estimated by fitting biexponential functions at the peak of the EPSC. Weighted decay time was calculated according to the following: $\tau_w = (\tau_1 * A_1 + \tau_2 * A_2)/(A_1 + A_2)$, where τ_1 and τ_2 represent the fast and slow decay time, with the corresponding amplitude fractions A_1 and A_2.
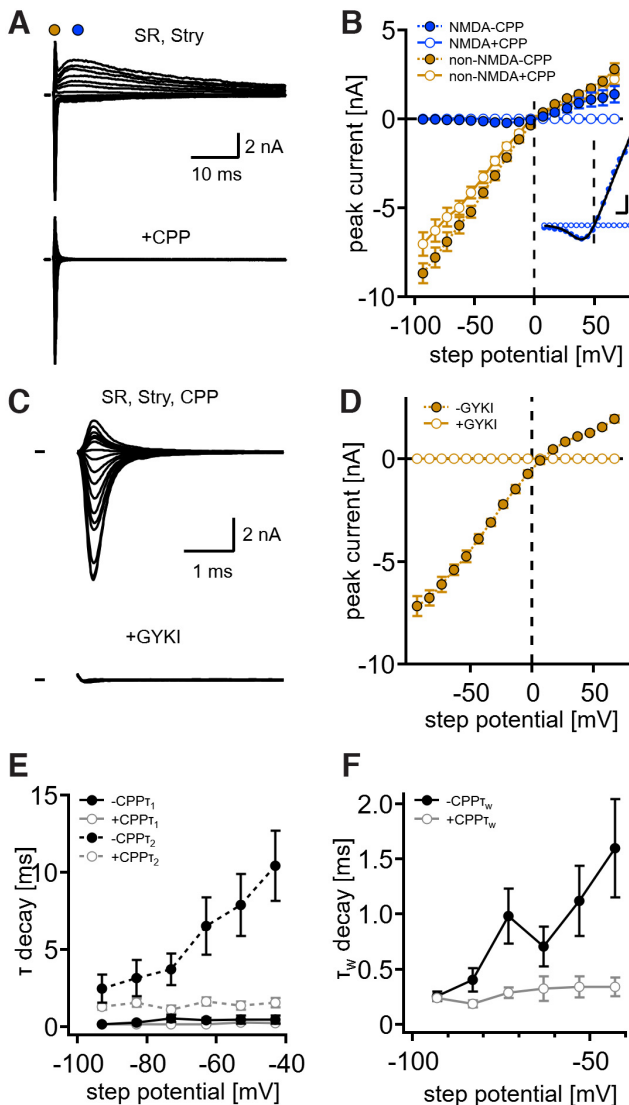
Figure 1. EPSCs at the endbulb of Held are AMPAR- and NMDAR-mediated. *A*, Top, Exemplary EPSCs of the VNLL synapse recorded at different step potentials (−93 to 67 mV, 10 mV increments) during single fiber stimulation with 2 mM extracellular Ca^{2+} from a P19 gerbil. Inhibitory inputs were blocked with 10 μM SR95531 and 1 μM strychnine. Non–NMDAR-mediated peak size was defined as the maximum current deflection at the beginning of the stimulus (orange symbol), and NMDAR-mediated component as the current size after 5 ms (blue symbol). Bottom, Addition of 10 μM R-CPP blocks the NMDAR-mediated component. *B*, I–V relationship of NMDAR- (blue) and non–NMDAR-mediated currents (orange), before and after R-CPP application (filled and open circles, respectively). Inset, Enlarged plot of the NMDAR-mediated I–V curve. A sigmoid Boltzmann fit (black) described the nonlinear relationship (V_{half} = −24.3 mV, V_{rate} = 23 mV). Calibration: 20 mV, 300 pA. *C*, Non–NMDAR-mediated current (top) and full elimination after application of the AMPAR antagonist GYKI-53655 (bottom). *D*, I–V relationship of non–NMDAR-mediated currents before and after GYKI-53655 application (filled and open circles, respectively). *E*, τ_1 and τ_2, calculated from biexponential fits to EPSC decays before and after R-CPP application. *F*, The average weighted decay time (τ_w), plotted against step potentials. *B*, *D–F*, Data are mean ± SEM. n = 7 (*A,B*), n = 6 (*C–F*). P21.2 ± 1.

In order to define the rate of the frequency-dependent STP, we stimulated afferent fibers with 20 pulse trains and frequencies ranging from 1 to 333 Hz, in physiological extracellular Ca^{2+} concentration (1.2 mM). The envelope current amplitudes of each pulse, calculated as the maximum current deflections from the baseline before stimulations, were normalized to the amplitude of the first EPSC. Paired-pulse ratio (PPR) was calculated as the ratio of the second to the first EPSC size, and steady state as the average STP ratio of the last three pulses.

Synapse model. To simulate synaptic trains in conductance clamp, we generated templates with linear AMPAR-and nonlinear NMDAR-mediated conductances. In order to estimate the nonlinear behavior of NMDARs, we fitted sigmoid Boltzmann curves in the I–V relationships of the NMDAR current and estimated the average half-activation voltage (V_{half} = −24.282 mV) and activation rate (V_{rate} = 23.046). During conductance clamp recordings, the injected current for simulated AMPAR (simAMPAR) and NMDAR (simNMDAR) conductances was individually calculated online (AMPAR: I_{AMPA} = G(t) (V_m − V_{rev}); NMDAR: I_{NMDA} = (V_m − V_{rev}) G(t)/(1 + exp[(V_{half} − V_m)/V_{rate}])). To assert possible contribution of simNMDAR conductance to output generation, every cell was challenged with only simAMPAR, and with simAMPAR plus simNMDAR EPSGs. Both templates were scaled in size between 15% and 100% of the average unitary EPSC. In this study, the average conductance of a unitary EPSC from a single terminal recorded in 1.2 mM extracellular calcium concentration was 78.9 nS. Action potential generation rate was analyzed for all EPSG paradigms.

To detect potential contribution of the slow simAMPAR component to action potential generation, EPSGs with stable τ_1 and τ_2, but with different amplitude ratios of A_2 to A_1, expressed as %, and ranging from 0 to 100 were generated. Twenty pulse EPSGs of frequencies between 10 and 400 Hz, with corresponding STP ratios were scaled and the success rate of action potential generation was determined. Additionally, the absolute refractory period of VNLL neurons was calculated, by injecting paired-pulse simAMPAR EPSG spikes, with or without NMDAR conductance, and with interstimulus frequencies between 100 and 2000 Hz.

To approach a more physiological state of synaptic transmission, 8-s-long EPSG templates were generated with custom-written functions in MATLAB (The MathWorks). EPSG generation incorporated AMPAR and NMDAR kinetics and frequency-dependent simulated STP (simSTP), as shown in Figures 1 and 2. Stimulation templates either excluded simSTP and contained only simAMPAR conductances ($EPSG_{AMPA}$ = A_0 * (A *(exp[(t − t_0)/tau_g] − exp[− (t − t_0)/tau_d])), where A_0=4.9152e-9, A = 237.295, tau_g = 1.3634e-4, tau_d = 1.3793e-4, and t_0 = 0.0011), or AMPAR and NMDAR conductances ($EPSG_{NMDA}$ = $EPSG_{AMPA}$ + A_0 * (A * (exp(t − t_0)/tau_g − exp(t − t_0) tau_d)), where A_0 = 4.9152e-9, A = 0.079, tau_g = 5.4651e-4, tau_d = 0.0172, and t_0 = 0.0013). The second set of templates incorporated a phenomenological model of simSTP, and was based either on simAMPAR or simAMPAR and simNMDAR conductances. Although the simSTP model includes physiological interpretable parameters, such as vesicle resource (R) and probability (P) of release, it should not be seen as a reflection of biophysical reality, simply owing to its restriction to a single vesicle pool and a single facilitatory term. Phenomenological models of that kind have been successfully used to simulate dynamical synaptic transmission under ongoing stimulation in other synapses (Markram and Tsodyks, 1996; Sen et al., 1996; Hanson and Jaeger, 2002; Gundlfinger et al., 2007; Hermann et al., 2009). The simulated amplitude A_n= P_nR_n on stimulus n was thereby calculated as product of release probability P and apparent pool size R of releasable vesicles with P_n = (f (p_{max} − P_{n-1}) + (P_{n-1} − p_0)) * exp(−dt/tau_d) + p_0 and R_n = R_0 + ((1 − P_{n-1}) * R_{n-1} − R_0) * exp(−dt/tau_R), where f = 0.987 is the facilitation factor, tau_d = 10.9 ms the time constant of decay of faciltation, tau_R = 1.07 s the time constant of pool replenishment, p_{max} = 0.0807 and p_0 = 0.0609 denote the bounds for P, and dt the interstimulus time between input n and n-1. Parameters were obtained from numerical minimum least square fits to the depression curves in Figure 2C. Interstimulus intervals dt were Poisson-distributed restricted to instantaneous frequencies between 1 and 800 Hz. As previously, each cell was injected with either simAMPAR alone, or with the addition of simNMDAR EPSGs, and template size was scaled between 20% and 120%. All experiments were repeated 3-10 times, and the results were averaged for each neuron.

Output success rate was defined as the ratio of supra-threshold events to the total number of delivered pulses, and action potential latency (see Fig. 7) as the duration between the pulse and action potential peak. Action potential latencies were either averaged across all supra-threshold events in response to each EPSG template, or individually
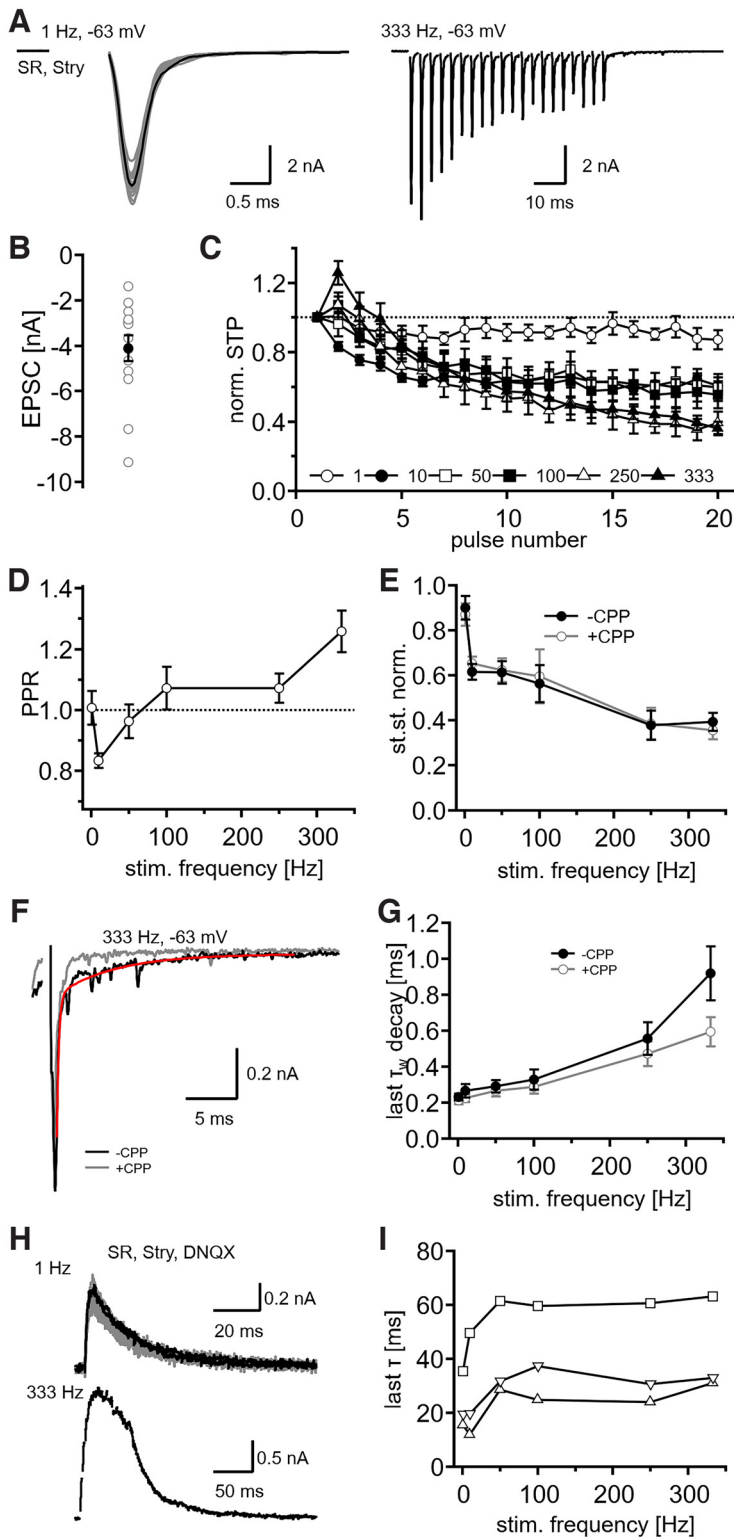
Figure 2. STP of the VNLL synapse. **A**, Left, EPSCs of a P22 VNLL neuron, evoked with a 20 pulse stimulation train of 1 Hz and 1.2 mM extracellular Ca^{2+}. For comparison, the first and last EPSCs are plotted as black traces. Right, EPSCs from the same neuron evoked with a 20 pulse stimulation train of 333 Hz. The neuron was held at −63 mV. **B**, Maximum EPSC size. Open circles represent individual synapses. Black circle represents average ± SEM. n = 14. **C**, Average STP of envelope EPSCs, normalized to the first EPSC size for stimuli of 1, 10, 50, 100, 250, and 333 Hz. **D**, PPR, as a fraction of the second to the first EPSC size. **E**, Normalized steady-state depression (st.st. norm.), plotted against stimulation frequency before and after *R*-CPP application (filled and open circles, respectively). **F**, The temporal decay of the last EPSC before and after *R*-CPP was calculated by fitting a biexponential function (red line) at the end of the stimulation trains. **G**, Weighted decay times (τ_w) of the last pulse were plotted against stimulation frequencies before and after *R*-CPP application (filled and open circles, respectively). **H**, Pharmacologically isolated NMDAR-mediated current evoked by stimulation trains of 1-333 Hz. Top, Twenty overlaid NMDAR-mediated EPSCs of 1 Hz trains. Bottom, NMDAR-mediated EPSCs evoked with 333 Hz train. Black traces represent the first and last EPSCs of the stimulation train. n = 3. **I**, The decay time (τ) of the last NMDAR-mediated EPSC plotted against stimulation frequencies. **B–E**, **G**, 1 Hz: n = 11; 10 Hz: n = 5; 50 Hz: n = 7; 100 Hz: n = 6; 250 Hz: n = 7; 333 Hz: n = 12. Data are mean ± SEM. P21.8 ± 0.4.

plotted against the maximum peak conductance of each pulse. Latency values from templates without STP were averaged and compared with latencies derived from templates with STP. The latency from the latter responses was averaged at conductance levels of ±5 nS from templates without STP. Frequency sensitivity of action potential generation was analyzed by pooling of all supra-threshold events within a bin of 100 Hz of stimulation frequencies. Output was furthermore normalized to the number of stimulations within the frequency bin (see Fig. 8).

Circuit simulations. We used the octopus cell model described by Rebhan and Leibold (2021) to generate model octopus cell spike trains for sound stimuli in a population with center frequencies between 1 and 10 kHz. In brief, the model uses a modified (Zilany-Bruce-Carney) periphery model (Zilany et al., 2009, 2014) adjusted to human parameters and feeds its output into a phenomenological octopus cell model, which primarily acts as a differentiator (Oertel et al., 2000). The obtained octopus cell spikes were then used as input to the synaptic dynamics described in the previous paragraph (AMPA+NMDA+/−STP). The synaptic inputs were then fed into a model VNLL cell, modeled as a leaky integrate and fire model with time constant 5 ms (Fischer et al., 2018), threshold of 0.25 mV × input resistance (in MOhms) and a prolonged refractory period of 10 ms to effectively model feedforward inhibition.

Data analysis and statistics. Electrophysiological data were analyzed with custom-written Igor Pro Version 7 (WaveMetrics) functions and further processed with Microsoft Excel. MATLAB R2016a (The MathWorks) software was used to generate the Poisson-distributed templates. For the results of Figure 1, a total of 13 neurons from 12 animals were recorded; and for Figure 2, 16 neurons from 15 further animals were analyzed. Figures 3 and 4 show data collected from 11 neurons and 5 gerbils, and from 10 neurons and 5 gerbils, respectively. Figure 5 shows data from 11 neurons and 3 animals, Figures 6-9 from 22 neurons from 12 gerbils. Statistical analysis was conducted with GraphPad Prism version 9.2.0. Datasets were tested for normal distribution using the Kolmogorov–Smirnov test. All data indicated normal distribution, except from the τ_1 values at −43 and −53 mV of Figure 1. The lack of normal distribution for these two data points is not relevant for the experimental design and interpretation of this study. Statistical comparisons were performed either with one-way ANOVA with *post hoc* Tukey test, or paired and unpaired multiple *t* tests, with Holm–Sidak correction. The significance level was set at 5%. Data are presented as mean ± SEM.

Results

Pharmacological composition of glutamatergic endbulb currents

Current components of the glutamatergic synaptic transmission at the VNLL endbulb in hearing gerbils of P21.5 ± 0.7 (range P18-P26, $n = 13$) were pharmacologically and electrophysiologically identified. To isolate glutamatergic currents, inhibitory GABA- and glycinergic inputs were blocked by application of 10 μM SR95531 and 1 μM strychnine, in a background of 2 mM extracellular Ca^{2+} concentration. Depending on the step potential, EPSCs showed dual components (Fig. 1A). To extract the distinct voltage-dependent contribution of glutamatergic currents, the peak at the beginning of the EPSC and the residual current 5 ms after this peak were quantified. Application of the NMDAR antagonist R-CPP selectively abolished the slow EPSC component, determined at 5 ms after the EPSC onset, confirming that the second component is mediated by NMDA currents (Fig. 1A). By plotting I–V curves for both non–NMDAR- and NMDAR-mediated currents (Fig. 1B), we showed that, even at hyperpolarized potentials < -73 mV, a small amount of current (~ 40 pA) permeates NMDARs. The inward NMDAR current was maximal at -23 mV with -0.22 ± 0.08 nA ($n = 7$). NMDAR-mediated currents reversed at 0 mV and showed outward rectification. To extract the degree of voltage-dependent Mg^{2+} unblocking of NMDAR-mediated currents, a sigmoid Boltzmann function was fitted to the I–V curve, with resulting half-activation voltage $V_{half} = -24.282$ mV and activation rate $V_{rate} = 23.046$ (Fig. 1B, inset). Non–NMDAR-mediated currents reversed at 0 mV and showed strong inward rectification, in agreement with earlier results (Kladisios et al., 2020). This suggests that mainly GluR2 lacking AMPARs known from other auditory brainstem nuclei (Geiger et al., 1995; Lujan et al., 2019; Franzen et al., 2020) are underlying the adaptation of rapid synaptic transmission. The maximal recorded non–NMDAR-mediated inward and outward currents were -8.67 ± 0.3 nA and 2.8 ± 0.2 nA recorded at step potentials of -93 and 67 mV, respectively ($n = 7$).

To assess whether the fast non-NMDAR component is exclusively driven by AMPAR-mediated currents, we applied 50 μM of the noncompetitive AMPAR antagonist GYKI, along with R-CPP, strychnine, and SR95537. The application of GYKI fully eliminated the EPSCs (Fig. 1C), as also seen in the I–V relationship of Figure 1D. Therefore, EPSCs at the endbulb are exclusively mediated by AMPAR and NMDARs.

Next, we analyzed the EPSC kinetics of inward currents before and after application of R-CPP, by fitting biexponential functions at the peak of the EPSCs (Fig. 1E). The fast decay time constant (τ_1) ranged between 0.16 and 0.52 ms with no voltage-dependent significant change between -93 and -43 mV, for either control condition or during R-CPP application (one-way ANOVA: -CPP, $F_{(6,35)} = 1.221$, $p = 0.319$, CPP, $F_{(6,35)} = 0.6966$, $p = 0.654$). Furthermore, τ_1 values did not change significantly in R-CPP (multiple paired t test, with Holm–Sidak correction, $p > 0.05$ for all step potentials), indicating that the first component is voltage-insensitive and
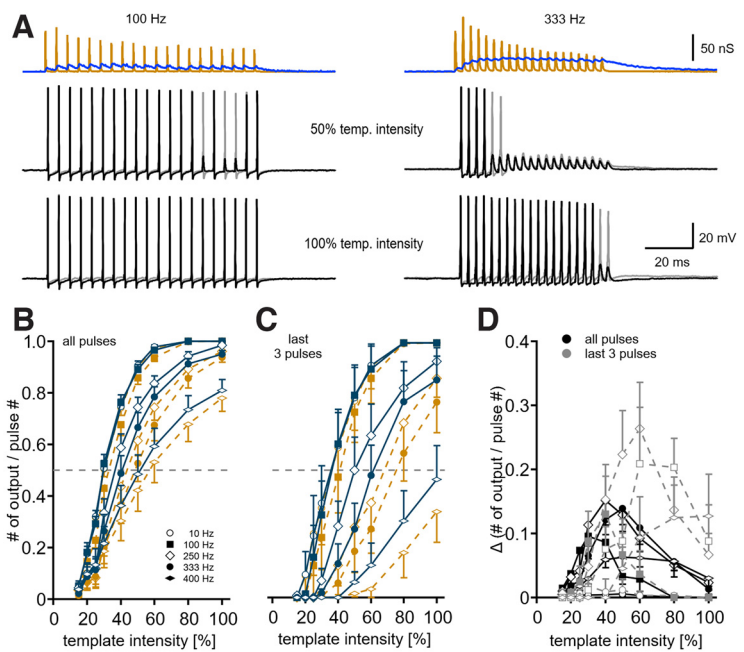

Figure 3. Impact of AMPAR- and NMDAR-mediated conductance on output generation during short stimulation trains. **A**, Linear simAMPAR (orange) and nonlinear simNMDAR (blue) conductance templates (EPSGs) with 20 pulses and frequencies between 10 and 400 Hz. Either simAMPAR EPSGs were injected alone or together with simNMDA EPSGs, and voltage responses were recorded. The voltage response to simAMPA EPSGs (black traces), and to simAMPA and simNMDA EPSGs (gray traces), is shown at two template intensities of 50% and 100%. **B**, Normalized output for either simAMPAR (orange symbols) or for simAMPAR and simNMDA EPSGs (petrol symbols) plotted against the injected template intensity according to stimulation frequency (symbol-coded). Gray lines indicate normalized output level of 0.5. **C**, Same as in **B**, but with the normalized averaged output of the last 3 pulses of each EPSG stimulation train. **D**, Influence of simNMDAR conductance on normalized output. The simNMDAR influence is depicted as the difference between the evoked output (recording with simNMDAR – recording without simNMDAR conductance) normalized to the pulse number as a function of stimulation intensity. Black symbols represent the overall normalized output difference. Gray symbols represent the difference of normalized output of the last 3 pulses in the stimulation train. Stimulation frequency was symbol-coded as in **B**. P31 ± 0.1, $n = 11$. Data are mean with one-sided SEM.

AMPAR-mediated. The slow decay time (τ_2) gradually increased significantly with more positive step depolarizations, from 2.5 ± 0.9 ms at -93 mV to 10.4 ± 2.3 ms at -43 mV (one-way ANOVA, $F_{(6,35)} = 7.004$, $p = 5.95\text{e-}5$). Application of R-CPP eliminated this increase and τ_2 remained unchanged through all potential steps (one-way ANOVA, $F_{(6,35)} = 1.648$, $p = 0.161$) (Fig. 1E). This voltage-dependent increase of τ_2 was significantly different > -53 mV between control and R-CPP (multiple paired t test, with Holm–Sidak correction, -53 mV, $p = 0.05$; -63 mV, $p = 0.023$). Even after blocking of NMDAR conductances, the AMPAR-mediated EPSC decay is composed of a fast and a slow time constant.

Combining the components of the EPSC decay time with the fractional decay, we extracted the weighted EPSC decay time τ_w $(\tau_1 * A_1 + \tau_2 * A_2)/(A_1 + A_2)$. τ_w increased in a voltage-dependent manner, with values of 0.25 ± 0.04 ms and 1.6 ± 0.44 ms at step potentials of -93 and -43 mV, respectively (one-way ANOVA: -CPP, $F_{(6,35)} = 5.42$, $p = 4.8\text{e-}4$), and did not significantly change after R-CPP wash-in (one-way ANOVA: -CPP, $F_{(6,35)} = 0.7322$, $p = 0.627$) (Fig. 1F). Overall, we showed that EPSCs at the endbulb of Held are AMPAR-driven, with a small but substantial contribution of NMDAR-mediated currents that persist even in mature gerbils.

Frequency-dependent STP

Ongoing synaptic activity can lead to history-dependent STP and thereby generate features, such as gain control
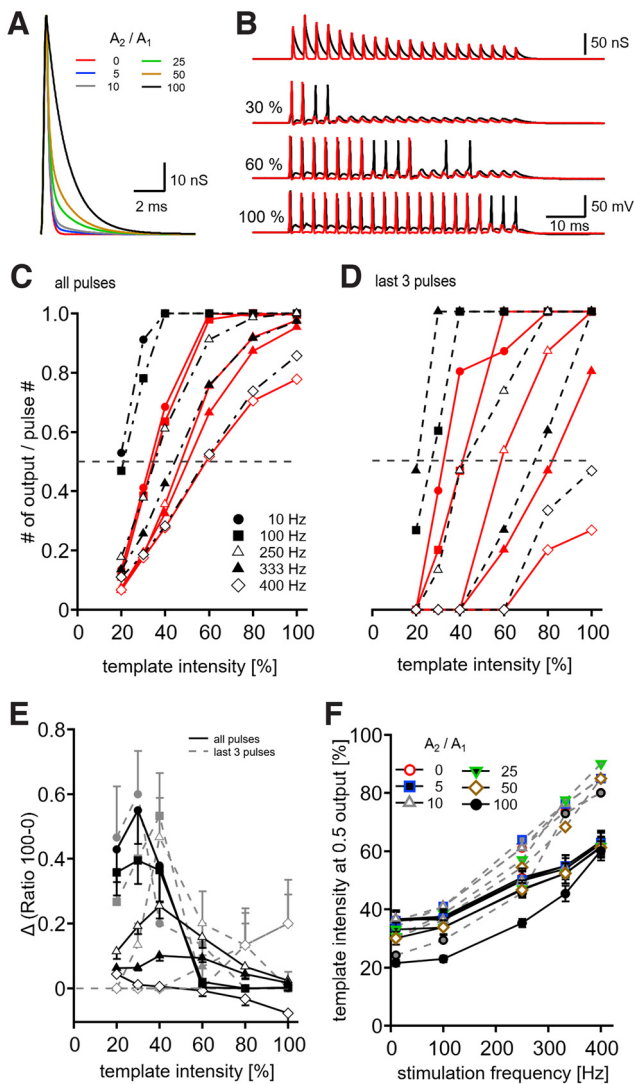
Figure 4. Impact of EPSC shape on output. **A**, VNLL AMPAR EPSGs with stable τ_1 and τ_2 (Fig. 1E), and varying A_2-to-A_1 fractions between 0% and 100%. **B**, Twenty pulse EPSG trains of varying stimulation frequencies, each consisting of the six A_2-to-A_1 fractions, were injected (top) and the voltage response was recorded for different template intensities. Red and black traces represent the extreme A_2-to-A_1 fractions of 0% and 100%, respectively. **C**, Normalized output, according to different A_2-to-A_1 fractions and stimulation frequencies. For clarity, only output of 0% and 100% A_2-to-A_1 fractions (red and black traces, respectively) are shown. Gray line indicates the normalized output of 0.5. Data are mean values. **D**, Same as in **C**, but with the normalized output of the last 3 pulses in the stimulation train. **E**, Difference of normalized output between A_2-to-A_1 of 100% and 0%. Solid lines indicate the overall output difference. Dotted lines indicate the output difference for the last 3 pulses in the stimulation train. Symbols mark frequencies, coded as in **C**. Data are mean and one-sided SEM. **F**, Template intensity corresponding to 0.5 of normalized output, plotted against train frequencies for the different A_2-to-A_1 fractions. Solid lines indicate cutoff values of all spikes. Dotted lines indicate steady state. Data are mean ± SEM. P30.6 ± 0.3, $n = 10$.

(Rothman et al., 2009; Pedroarena, 2020), temporal filtering (Fortune and Rose, 2001; Kuba et al., 2002; Cook et al., 2003), and sensory adaptations (Chung et al., 2002). To assess the STP at the endbulb synapse, we stimulated single afferent fibers with 20 pulse stimulation trains and frequencies between 1 and 333 Hz. During stimulation, neurons were held at −63 mV and inhibitory inputs were pharmacologically blocked. To approximate physiological release probability, the external solution contained 1.2 mM Ca^{2+} (Borst, 2010).
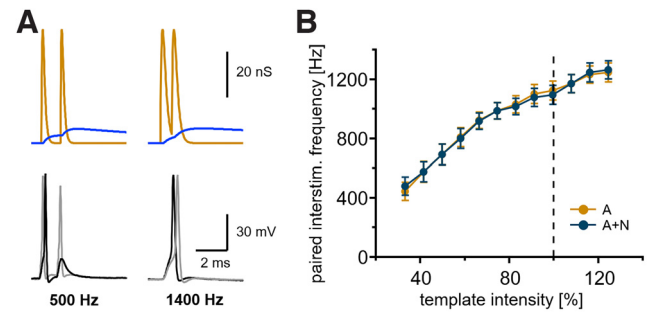

Figure 5. Absolute refractory period of VNLL neurons. **A**, Equally sized, paired-pulse simAMPAR and simNMDAR EPSGs (orange and blue, respectively) with varying template intensity and interstimulus duration were injected. Two EPSGs of 500 and 1400 Hz, and the corresponding voltage responses are exemplified. **B**, Temporal discrimination, as the frequency where both pulses generated supra-threshold responses, was plotted against template intensity. Data are mean ± SEM. P29.7 ± 0.1, $n = 11$.

The amplitude of EPSCs during a 20 pulse stimulation train depended on the stimulation frequency and pulse number. At 1 Hz intervals, EPSC amplitudes remained stable; while at higher frequencies, EPSC amplitudes significantly depressed after an initial increase (Fig. 2A). To analyze the STP, the envelope EPSC amplitudes were normalized to the first EPSC amplitude, which at physiological external Ca^{2+} concentrations was −4.12 nA (Fig. 2B). Normalized STP revealed an average frequency-dependent interplay between initial facilitation and depression (Fig. 2C). Stimulation frequencies <50 Hz showed no facilitation and low synaptic depression. For frequencies of ≥100 Hz, the second and eventually two more following EPSCs increased in amplitude, followed by depression (Fig. 2C). The data from Fig. 2C were used to fit the parameters of our phenomenological STP model that was used for further conductance clamp stimulations.

Synaptic facilitation and depression were quantified by analyzing PPR and relative steady-state plasticity. PPR analysis revealed that the synapses facilitate >100 Hz (Fig. 2D). Steady-state depression increased in a frequency-dependent manner (Fig. 2E). At the end of the 20 pulse train, EPSC amplitude dropped to 89.9% and 61.5% of the initial EPSC for frequencies of 1 and 50 Hz, respectively, and to 39.3% for 333 Hz. Blocking NMDARs with R-CPP had no significant effect on steady-state depression (multiple paired t test, with Holm–Sidak correction, $p > 0.05$ for all frequencies) (Fig. 2E).

In order to examine the influence of stimulation frequencies on the decay of EPSCs, the peak of the last EPSC was fitted with a biexponential function (Fig. 2F). The weighted decay time increased according to stimulation frequency, starting with 0.2 ± 0.02 ms at 1 Hz, and reaching 0.9 ± 0.15 ms at 333 Hz. Blocking NMDARs decreased τ_w at high stimulation frequencies of 333 Hz (multiple paired t test, with Holm–Sidak correction, frequencies 1-250 Hz; $p > 0.05$; 333 Hz, $p = 0.0034$) (Fig. 2G), indicating that NMDAR-mediated current build-up is present during high-frequency stimulation trains.

To obtain further insights into the frequency-dependent NMDAR-mediated current build-up and kinetics, non-NMDAR currents were blocked by DNQX, and NMDAR-mediated currents were recorded at 37 mV at varying stimulation frequencies (Fig. 2H). Stimuli of higher frequencies elicited build-up currents. Furthermore, the decay time (τ) of the last NMDAR-mediated EPSC was measured by fitting an exponential function. In all three recorded neurons, an increase in τ was detected for

frequencies up to 50 Hz. Above 50 Hz, the NMDAR-mediated current decay remained constant, between 30 and 60 ms (Fig. 2*I*, *n* = 3). Last, the 20%-80% rise time of the NMDAR-mediated current was calculated as 1.29 ± 0.03 ms (*n* = 8).

Impact of distinct synaptic properties on action potential generation

After having characterized AMPAR- and NMDAR-mediated EPSCs and their STP, we sought to gain insights into their functional contributions. Therefore, we decomposed their synaptic components and measured output generation by recording voltage responses of VNLL neurons in conductance clamp. Linear simAMPAR, and nonlinear simNMDAR conductance templates (EPSGs) of 20 pulses and frequencies between 10 and 333 Hz were created, and included a simSTP template according to the average initial EPSC amplitude, decay kinetics, STP, and voltage-dependent activation, as described in Figures 1 and 2. Additionally, 20 pulse EPSG trains of 400 Hz were generated, and their STP was calculated by fitting a linear function to the STP rate of each pulse for frequencies between 10 and 333 Hz. The average AMPAR conductance of a single synaptic input, evoked in 1.2 mM extracellular Ca^{2+} concentration, was 78.9 nS. EPSG templates were scaled between 15% and 100% of initial conductance (Fig. 3*A*).

The action potential generation, defined as output, was normalized to the number of stimulation pulses and depended on the stimulation frequency and template intensity (Fig. 3*B*). Failures in output generation occurred in response to EPSG frequencies only >250 Hz. Adding simNMDAR conductances increased output significantly between 30% and 60%, as well as 30% and 80% of conductances equal to a single endbulb EPSC for 250 Hz and >333 Hz, respectively (multiple paired *t* test, with Holm–Sidak correction) (Fig. 3*B*). Since most failures occurred at the end of a stimulation train, the output from the last three pulses of each stimulation frequency was separately analyzed (Fig. 3*C*). Compared with the overall output, the steady-state output decreased, especially in higher stimulation frequencies. Here, simNMDAR EPSGs significantly amplified output for trains of 250 and 333 Hz and stimulus intensities between 40% and 80%, as well as for 400 Hz stimulations between intensities of 80% and 100% (multiple paired *t* test, with Holm–Sidak correction) (Fig. 3*C*). To illustrate the NMDAR-mediated contribution, we determined the difference between the output with and without simNMDAR EPSGs (Fig. 3*D*). NMDAR-dependent amplification was more prominent in high frequencies and at steady state, and is likely be attributed to the residual NMDAR current build-up in ongoing high-frequency stimulations.
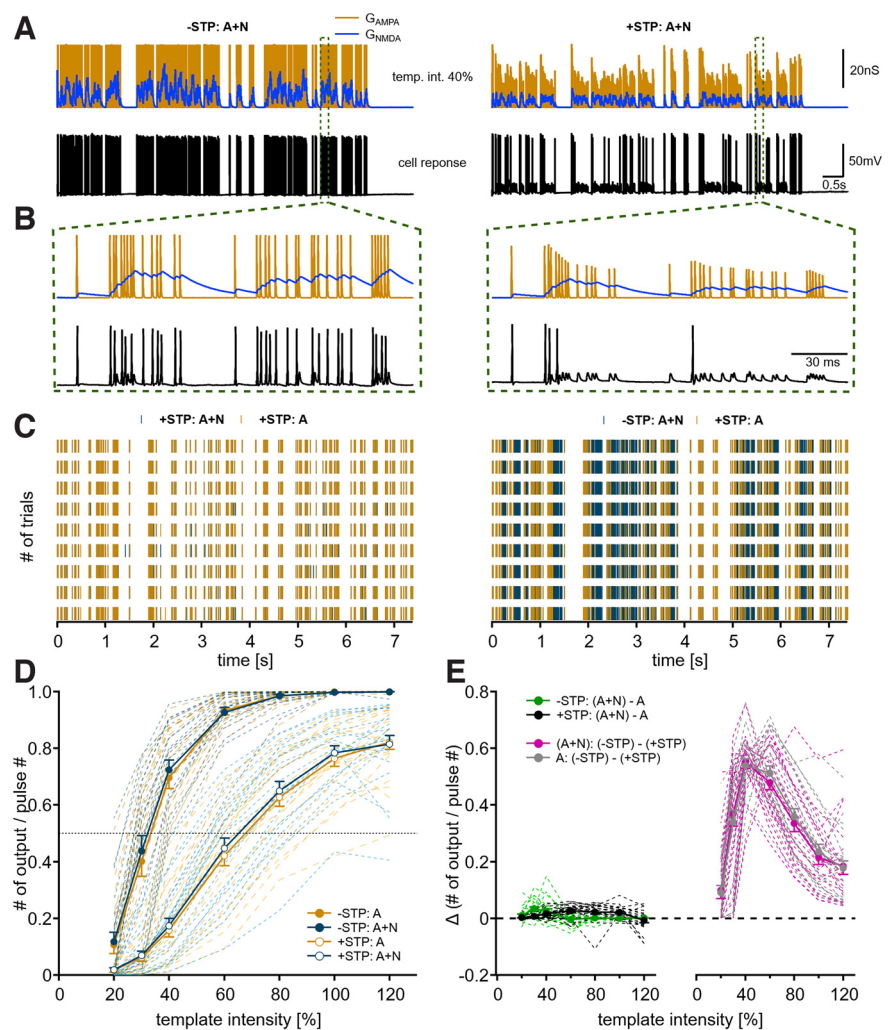
Figure 6. Poisson-distributed stimulation trains simulate physiological synaptic inputs. *A*, Long EPSG trains, with Poisson-distributed interstimulus frequencies between 1 and 800 Hz for both simAMPAR and simNMDAR conductances (orange and blue traces, respectively). Voltage response to simAMPAR EPSGs, or simAMPAR with simNMDA EPSGs recorded in a VNLL neuron. Maximum EPSG of each pulse either remained constant (left) or varied according to the modeled simSTP (right). *B*, Enlargement of the dotted area of *A*. Scale of y axis as in *A*. *C*, Each line indicates a single action potential in response to the Poisson-distributed EPSG train, according to trial number. Left, Responses to simAMPAR and simNMDAR EPSGs with simSTP (petrol) and simAMPAR EPSGs with simSTP (orange). Right, Responses to simAMPAR and NMDAR EPSGs with and without STP (orange and petrol, respectively). *D*, The normalized output of the four different EPSG template paradigms was plotted against stimulus intensity of the first EPSG. Orange and petrol symbols represent normalized output from simAMPAR, and simAMPAR and simNMDAR EPSGs, respectively. Filled circles represent EPSGs without STP. Open circles represent EPSGs with simSTP. Dotted lines indicate normalized output from individual neurons. Dotted line indicates the 0.5 level of normalized output. *E*, The difference of the normalized output between EPSG paradigms was plotted against template intensities (recording with simSTP – recording without STP and recording with simNMDAR – recording without simNMDAR). Left, The normalized output contribution of simNMDA for EPSGs with and without STP (black and green lines). Right, The normalized output contribution of simSTP for trains with simAMPAR, and simAMPAR and simNMDAR EPSGs (gray and magenta lines). Dotted lines indicate difference of individual neurons. Solid lines indicate average. P24.7 ± 0.8, *n* = 22.

Previous studies in auditory brainstem neurons have shown that a stimulus waveform influences action potential current thresholds (Cathala et al., 2003; Couchman et al., 2010; Ammer et al., 2012; Lehnert et al., 2014; Franzen et al., 2015; Cao and Oertel, 2017; Kladisios et al., 2020; Bondy et al., 2021). Since VNLL EPSCs exhibited biexponential decay that persisted after NMDAR block (Fig. 1*E*), we investigated a potential functional role of the second AMPAR component with regard to output generation. For that purpose, we created 20 pulse simAMPAR EPSG trains of different frequencies (10-400 Hz), with the previously determined decayed time constant (τ_1 = 0.165 ms,

τ_2 = 2.457 ms) and varied the amplitude fractions A_2-to-A_1 (Fig. 4A). Under physiological conditions, this fraction approximated 10% in an average endbulb EPSC. Train conductances were scaled from 20% to 100% of a single synaptic input and the supra-threshold output generation was recorded and normalized to the stimulation pulse number (Fig. 4B). For better visualization, only results from 0% and 100% of amplitude fractions are given in Figure 4C.

Overall, the average output significantly differed between 0% and 100% A_2-to-A_1 fractions for most intensities at frequencies <400 Hz (multiple paired t test between A_2-to-A_1 fraction 0 and 100%, with Holm–Sidak correction, 10 Hz, $p < 0.05$ for intensities 20%-40%; 100 Hz, $p < 0.05$ for intensities 20%-40% and 100%; 250 Hz, $p < 0.05$ for intensities 20%-60%; 333 Hz, $p < 0.05$ for intensities 20%-80%; 400 Hz, $p < 0.05$ for intensities 20% and 100%) (Fig. 4C). The average output at steady state differed in a similar manner (multiple paired t test between amplitude fraction 0 and 100%, with Holm–Sidak correction, 10 Hz, $p < 0.05$ for intensities 20%-30%; 100 Hz, $p < 0.05$ for intensities 40%; 250 Hz, $p < 0.05$ for intensity of 40%; 400 Hz, $p < 0.05$ for intensity of 100%) (Fig. 4D). To illustrate the impact of altered A_2-to-A_1 fractions, we plotted the differences in output between 100% and 0% (Fig. 4E). This illustration revealed that 100% A_2-to-A_1 decaying EPSGs led to increased output, especially at intensities <80%. To further compare the output from all six simAMPAR EPSG shapes, we interpolated the average template intensity that produced a postsynaptic output of 0.5, as depicted in Figure 4C, D. For all stimulation frequencies, the template intensity at 0.5 output did not statistically differ for amplitude fractions between 0%, 5%, and 10% (one-way ANOVA, $p > 0.05$; Fig. 4F). For larger amplitude fractions, stimulation frequencies <250 Hz induced significant alterations in the stimulus intensity that led to an output of 0.5 (one-way ANOVA with *post hoc* Tukey test; 10 Hz, $p = 0.025$; 0% vs 100%, $p = 0.005$; 5% vs 100%, $p = 0.0075$; 10% vs 100%, $p = 0.0039$; 100 Hz, $p = 0.047$; 0% vs 100%, $p = 0.0302$; 5% vs 100%, $p = 0.0421$; 250 Hz, $p = 0.0446$; 0% vs 100%, $p = 0.0372$). Similar findings were extracted from the steady-state output analysis of the last three pulses (one-way ANOVA with *post hoc* Tukey test; 10 Hz, $p = 0.0172$; 0% vs 100%, $p = 0.0254$; 5% vs 100%, $p = 0.0254$; 10% vs 100%, $p = 0.0254$; 100 Hz, $p = 0.0041$; 0% vs 100%, $p = 0.0149$; 5% vs 100%, $p = 0.0065$; 10% vs 100%, $p = 0.0065$; 250 Hz, $p = 0.0176$; 0% vs 100%, $p = 0.0175$; 5% vs 100%, $p = 0.0216$; 333 Hz, $p = 0.9402$; 400 Hz, $p = 0.8629$) (Fig. 4F). Together, at physiological relevant A_1-to-A_2 ratios of ∼10%, the slow simAMPAR conductance component did not influence supra-threshold output generation.

Octopus cells can produce high firing rates of up to 800 Hz *in vivo* (Rhode and Smith, 1986; Oertel et al., 2000). Whether their target, the VNLL neurons, are able to retain this high temporal resolution is unclear. To test the absolute refractory period of VNLL neurons *in vitro*, we injected paired-pulse simAMPAR EPSGs, with and without simNMDAR EPSGs, with interstimulus frequencies between 100 and 2000 Hz. The intensity of these equally sized paired-pulse stimulations was scaled between 30% and 120% of a single endbulb EPSG (Fig. 5A). The frequency at which neurons started to respond suprathreshold to both pulses in the pair was averaged (Fig. 5B). Temporal discrimination of paired-pulses correlated with the stimulation intensity. At 30% stimulation intensity, the absolute refractory period was 478 Hz; and at 100% intensity, it reached 1092 Hz. simNMDAR conductance did not play a significant role in paired-pulse discrimination (paired t test, all intensities; $p > 0.05$). We conclude that VNLL endbulb

synapses reliably differentiate paired-pulse inputs of the full frequency range generated by octopus neurons.

Spike generation and synaptic fidelity from a physiologically stimulated endbulb

The previous results documented the fidelity of input–output functions with regard to different simAMPAR conductances and kinetics, as well as the contribution of the simNMDAR component, with standard 20 pulse trains at a resting synapse. Under physiological conditions, however, synapses show spontaneous activity. To mimic physiological activity, we simulated synaptic input conductances over a large range of Poisson-distributed frequencies, up to 800 Hz. The applied conductance train varied by removing or adding simSTP, the simNMDAR contribution, and the initial intensity (Fig. 6A,B). The voltage response to these conductance trains was analyzed (Fig. 6C), and the action potential number and timing were quantified.

We determined the normalized output for the different conductance paradigms in a stimulus intensity-dependent manner. For this purpose, the number of action potentials was counted and normalized to the number of EPSGs in the conductance train (Fig. 6D). Thus, a normalized output of 1 indicates that each EPSG led to an action potential. When simSTP was eliminated from the templates, even stimulation intensities <80% of a single endbulb input led to a normalized output of one. The removal of simSTP shifted the output leftward. Thus, the half-value of the normalized output was reached already at 33.5 ± 1.4% of a single input, corresponding to 26.4 nS, on average. When simSTP was included, the half-maximal output was found at 66.7 ± 2.8% (52.6 nS) of a single input. Importantly, with simSTP failures emerged, even at intensities resembling a single input. This indicates that VNLL endbulbs do not operate error-free under physiological conditions. The presence of simNMDAR conductance shifted the normalized output leftwards, both for templates without and with simSTP. To illustrate the effect of simSTP and simNMDA conductance on action potential generation in physiological relevant stimulations, we pairwise subtracted the normalized output (Fig. 6E). With and without simSTP, the simNMDAR conductance led to a small but significant increase in action potential generation at various stimulation intensities (with simSTP: multiple paired t test, with Holm–Sidak correction, 30%: $p = 0.034$; 40%: $p = 0.0019$; 60%: $p = 3.3e-4$; 80%: $p = 0.027$; 100%: $p = 0.0019$; without simSTP: multiple paired t test, with Holm–Sidak correction, 30%: $p = 2.5e-e$; 40%: $p = 0.021$). simSTP was by far the most prominent factor in altering the output (Fig. 6E, right). With or without simNMDA conductance, simSTP significantly reduced the output at all stimulation intensities (multiple paired t test, with Holm–Sidak correction, $p < 0.05$ for all intensities). Together, simSTP appears to exert a strong filter on input–output functions in the VNLL, while simNMDA conductance can promote action potential generation at medium intensity levels.

As temporal fidelity is suggested to be a hallmark feature of VNLL neurons (Covey and Casseday, 1991; Zhang and Kelly, 2006a; Liu et al., 2014; Recio-Spinoso and Joris, 2014), we analyzed the overall action potential latency in our conductance trains as a function of stimulation intensity from the four different stimulation conditions (Fig. 7). The overall action potential latency decreased with increasing conductance intensity for all four stimulation paradigms (Fig. 7A). To quantify the effects of simSTP and simNMDAR conductance on latency in more detail, we subtracted the latencies between the different conditions (Fig. 7B). simNMDAR conductance barely affected latency (multiple
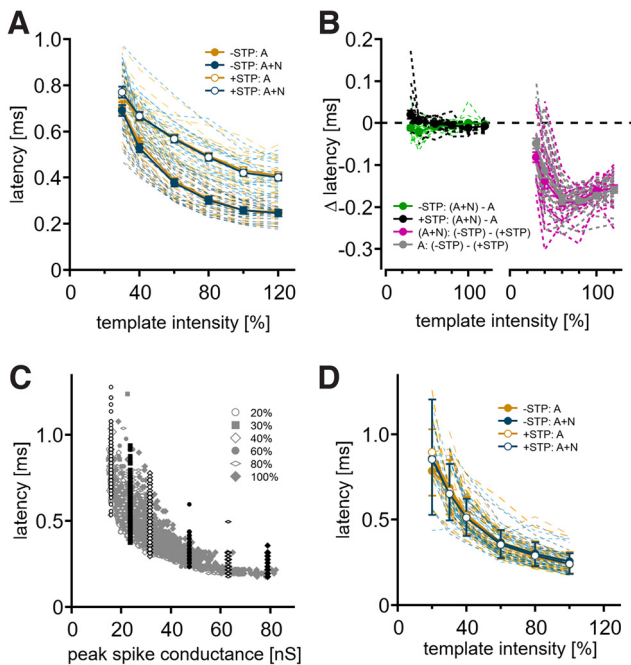
Figure 7. Temporal fidelity of the VNLL synapse during physiological train stimulation. ***A***, Average action potential latencies evoked by Poisson-distributed EPSG trains. Symbols as in Figure 6D. Solid lines indicate mean ± SEM. ***B***, The difference of action potential latency between EPSG paradigms (recording with simSTP − recording without STP and recording with simNMDAR − recording without simNMDAR) plotted against template intensity. ***C***, Individual action potential latencies of EPSGs with simSTP, plotted against the corresponding conductance peak of each stimulus, pooled from each template intensity. Latencies from all stimuli obtained from EPSGs without STP overlaid according to their conductance peak. All data originate from a single neuron. ***D***, Comparison of action potential latencies between matched template intensities. Latencies from EPSGs without STP were averaged across neurons, and latencies from EPSGs with simSTP were pooled and averaged at a level of ±5 nS from the maximum simAMPAR peak conductance of the former. Data are mean ± SEM. Symbols as in ***A***.

paired *t* test, with Holm–Sidak correction, 30%: *p* = 0.0024, 40%: *p* = 4.6e-5). simSTP led to a significant increase in latency (multiple paired *t* test, with Holm–Sidak correction, *p* < 0.05 for all intensities) that was most prominent between 60% and 100% of an average endbulb stimulation intensity.

So far, we have analyzed the average latency of all action potentials in a stimulation train as a function of the conductance intensity of the initial EPSG size. Since EPSG peak conductance varies during STP, we next analyzed the individual action potential latency in respect to the corresponding conductance peak within the stimulation train. Figure 7C exemplifies latency data recorded from a single neuron from trials of different initial EPSG conductance. The latency derived from action potentials stimulated with simSTP showed a continuous decline in relation to increasing individual peak EPSG sizes. When simSTP was excluded, latency values showed a range of latencies at the chosen peak conductance (Fig. 7C). The latencies derived from templates with and without simSTP overlaid. To disentangle the contribution of simNMDAR and simAMPAR conductance and simSTP on latencies, latencies were averaged across cells and statistically compared. Latencies from templates without simSTP were averaged, as in Figure 7A, and those from templates, including simSTP, were binned at ±5 nS from the corresponding conductance of the templates without simSTP (Fig. 7D). The averaged latencies declined with increasing stimulation intensity, and neither simNMDAR conductance nor simSTP significantly altered this relationship (multiple paired and unpaired *t* tests,

p > 0.05 for all combinations). Thus, action potential latency is a function of AMPAR EPSG size and not history-dependent, or modified by the NMDAR currents at the VNLL endbulb.

Above, we showed that the overall supra-threshold output and latency in our stimulation trains depended on the initial intensity and on the EPSG size. The EPSC size that underlies our EPSG templates shows a frequency-dependent STP. In addition, action potential generation is frequency-dependent. To illustrate and segregate the effects of frequency dependence of STP and action potential generation, we pooled the voltage responses according to 100 Hz bins of stimulation frequency within the conductance train (Fig. 8). The normalized output showed a strong frequency dependence for all four stimulation paradigms that was dependent on the initial EPSG size (Fig. 8A). The frequency-dependent loss of output was more severe when simSTP was included in the stimulation (Fig. 8A, compare left and right). Thus, simSTP strongly filters for action potential generation. For all frequencies, the addition of simNMDA increased the output (Fig. 8A, compare open and closed symbols). To quantify these differences, the output for select binned frequencies (100, 300, 500, and 700 Hz) was plotted versus the initial stimulus intensity (Fig. 8B). From these relations, we extracted the EPSG intensities that led to a 0.4 normalized output and plotted them against their respective binned stimulation frequencies (Fig. 8C). This allowed us to segregate the filter effects of STP from the action potential generator. At all frequencies, inclusion of simSTP required between 1.5 and 2.5 times more stimulation intensity to drive the same output (multiple paired *t* test, with Holm–Sidak correction, only simAMPAR EPSGs, 100 Hz, *p* = 1.4e-7, 300 Hz, *p* = 6.5e-11, 500 Hz, *p* = 6.9e-13, 700 Hz, *p* = 7.1e-14, simAMPAR and simNMDAR EPSGs, 100 Hz, *p* = 9.8e-8, 300 Hz, *p* = 1.97e-11, 500 Hz, *p* = 1.1e-12, 700 Hz, *p* = 3.9e-13). Addition of simNMDAR conductance lowered the required stimulus intensity for a 0.4 normalized output during frequencies of 300 and 500 Hz when simSTP was present (multiple paired *t* test, with Holm–Sidak correction, without simSTP, 300 Hz, *p* = 0.034, 500 Hz, *p* = 0.019; with simSTP, 300 Hz, *p* = 0.0067, 500 Hz, *p* = 1.5e-5), but not otherwise (multiple paired *t* test, with Holm–Sidak correction, without simSTP, 100 Hz, *p* = 0.28, 700 Hz, *p* = 0.38; with simSTP, 100 Hz, *p* = 0.15, 700 Hz, *p* = 0.24). The steepness of the relation between required EPSG size and stimulation frequency was a measure for the sensitivity of the filter and was larger when simSTP was included compared with when it was excluded (paired *t* test, simAMPA EPSG without simSTP vs simAMPA EPSG with simSTP, *p* = 4.67e-5, simAMPAR and simNMDAR EPSGs without simSTP vs simAMPAR and simNMDAR EPSGs with simSTP, *p* = 1.7e-4; unpaired *t* test, simAMPAR EPSG without simSTP vs simAMPAR and simNMDAR EPSGs without simSTP, *p* = 0.827, simAMPAR EPSG with simSTP vs simAMPAR and simNMDAR EPSGs with simSTP, *p* = 0.66). The steepness across the same binned stimulus frequency translated into a dynamic range. Thus, the dynamic range was ∼2.5-fold increased when simSTP was included compared with the action potential generator alone. Together, simSTP generated an efficient filter for action potential generation over a large range of stimulation intensities, while simNMDA conductance slightly counteracted this filter specifically in the mid-frequency range.

So far, we have analyzed the action potential output with respect to the binned interstimulus frequencies from the EPSG stimulation train. Some action potentials were, however, generated after failures; therefore, the frequency of supra-threshold output did not match the input frequency and this distinction remains so far undescribed. To gain insights into the frequency
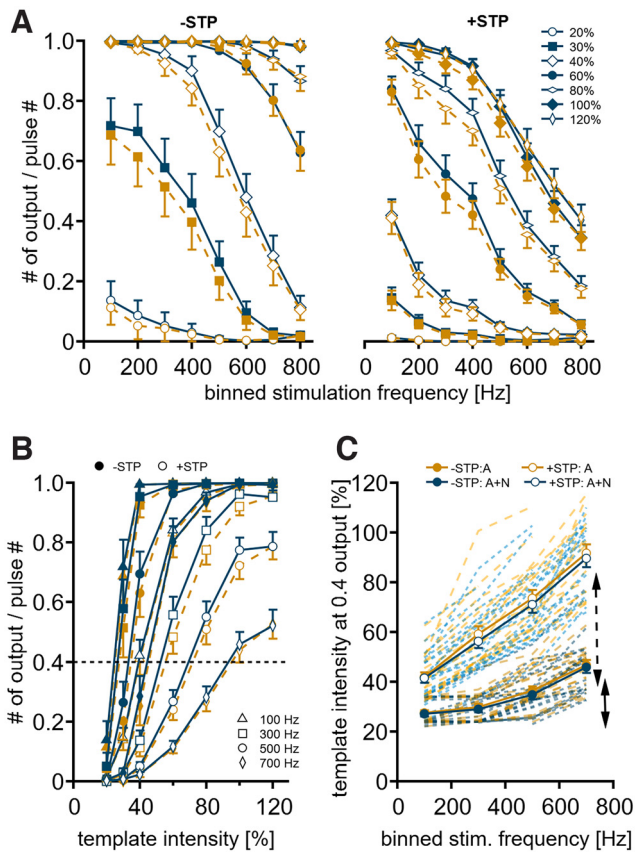
Figure 8. STP suppressed and NMDAR conductance facilitated frequency-dependent output size. ***A***, Normalized output of EPSGs without (left) and with simSTP (right), binned at 100 Hz steps. Orange symbols represent output from stimulations with simAMPAR EPSGs. Petrol symbols represent output from stimulations with simAMPAR and simNMDAR EPSGs. ***B***, Normalized output of 100, 300, 500, and 700 binned frequencies compared across template intensities, for simAMPAR (orange lines) and simAMPAR with simNMDAR EPSGs (petrol lines). Filled circles represent normalized output from EPSGs without STP. Open circles represent normalized output from EPSGs with simSTP. Dotted gray line indicates normalized output level of 0.4. ***C***, Template intensity required to evoke the level of 0.4 normalized output of single neurons (dotted lines) and as average (solid lines) for all stimulation paradigms as a function of stimulation frequency. Colors and symbols are as in Figure 7*A*. Arrows indicate the dynamic range of template intensities across stimulation frequency. Data are mean ± one-sided SEM.

Figure 9. Action potential generation is facilitated at specific frequencies. ***A***, Comparison of EPSG input (top) and resulting output frequencies (Δt, bottom) in a segment of Poisson-distributed templates. Arrows indicate the determination of the output frequency. ***B***, The number of binned output frequencies compared with the number of binned input frequencies for all EPSG paradigms as a function of stimulation frequency. Frequency bins were 100 Hz. Orange symbols represent simAMPAR EPSGs. Petrol symbols represent simAMPAR and simNMDAR EPSGs. ***C***, ***D***, Maximum relative output (***C***) and the binned frequency where this maximum occurred (***D***) according to template intensity. Data are mean ± one-sided SEM.

of output generation of VNLL neurons, we extracted the time between successfully evoked action potentials (Fig. 9*A*). First, the numbers of input and output events were binned in 100 Hz intervals. Second, a ratio of these values was calculated (Fig. 9*B*; number of outputs at a given binned frequency divided by the number of inputs of the same binned frequency) and plotted against the corresponding frequency bin. A frequency-specific output–input ratio of 1 indicates that a neuron responded to the input frequency with the same overall output frequency. Values <1 contained fewer events at this specific frequency compared with the stimulation input frequency. Conversely, values >1 indicated more outputs at a specific frequency compared with the same input frequency. When simSTP was removed and high stimulation intensities (≥100%) were applied, each input led to an output (success rate of 1) for each input frequency in the stimulation train (Fig. 9*B*, left). For binned input frequencies <400 Hz, the output–input ratio reached values >1 for stimulus intensities of 40%-60% without simSTP and for 80%-120% with simSTP. The values >1 indicated that frequency-specific output–input ratio <400 Hz were enhanced by skipping supra-
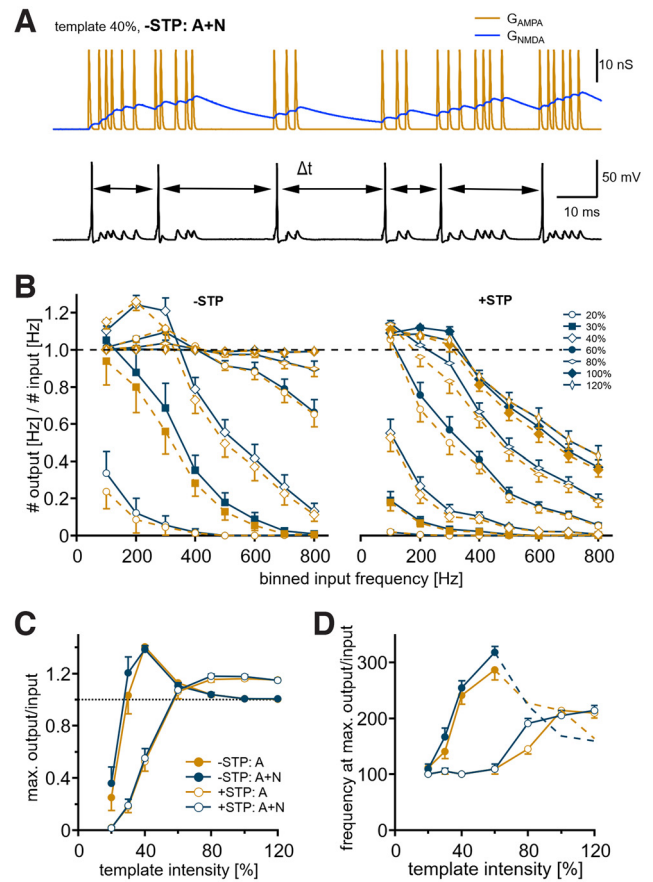
threshold responses during higher input frequencies. For all other frequency conditions, VNLL neurons generated less output and thus produced a frequency-specific output–input ratio <1. Overall simNMDA conductance increased the frequency-specific output–input ratio for most binned input frequencies <800 Hz, when simSTP was included (multiple paired *t* test, with Holm–Sidak correction, 40%: 200-400 Hz; 60%: 200-600 Hz; 80%: 200-700 Hz; 100%: 100-700 Hz; *p* < 0.05). Thus, simNMDAR conductance amplified output generation and allowed higher output rates. The maximum values of the filter functions in Figure 9*B* were determined for each stimulus intensity (Fig. 9*C*). Without simSTP, the maximal frequency-specific output–input ratio was found at 40% of stimulation intensity with a value of 1.4, indicating that output numbers are enhanced at a specific frequency. For stimulations containing simSTP, the maximal frequency-specific output–input ratio reached ~1.2 for stimulation intensities >60% of an average VNLL endbulb size. Thus, at physiological input intensities, simSTP enhanced specific output frequencies while others were suppressed. simNMDAR conductance had no effect (multiple paired *t* test, with Holm–Sidak correction, *p* > 0.05). Finally, we determined the frequency at which the maximal frequency-specific output–input ratio occurred (Fig. 9*D*). When simSTP was removed, the

maximal frequency-specific output–input ratio was largest at ~300 Hz input frequency at stimulation intensities of 60% of an average VNLL endbulb. In the presence of simSTP, the maximum frequency-specific output–input ratio was given at ~200 Hz input frequency for stimulation intensities >80%. Thus, STP limits the maximal frequency-specific output–input ratio and thereby promotes action potential generation to stimulation onsets <200 Hz.

STP supports invariance of VNLL output

To assess whether the conclusions about stimulus filtering properties of STP from our *in vitro* recordings can translate to more natural sound stimulus situations, we used a computational model of the octopus pathway (Rebhan and Leibold, 2021) and used the simulated spike output produced by the model as input to the synaptic dynamics described here. In summary, octopus cell model spikes were convolved with AMPAR and NMDAR EPSC waveforms (Figs. 1, 2); and when implemented, the amplitudes underwent STP dynamics as described in Figure 2. As sound input to the model, we used a sentence from a male speaker obtained from a free audiobook (*The Adventures of Huckleberry Finn*) at various sound pressure levels (for 55 dB SPL, see Fig. 10A). The synaptic currents (Fig. 10B, blue lines) were then used as input to a leaky integrate and fire model with time constant of 5 ms, resembling that of VNLL neurons (Franzen et al., 2015; Kladisios et al., 2020). To effectively model feedforward inhibition to the model neuron, the threshold 0.25 mV × input resistance (in MOhms) and a prolonged action potential refractory period of 10 ms were implemented. Visual inspection of the raster plots (Fig. 10B) revealed a general increase of activity with increasing sound pressure level, which was less pronounced in the presence of STP compared with its absence. Quantitative comparison of the overall spike counts (Fig. 10C) corroborated this observation. To ensure that the spiking patterns retained greater similarity over time, we computed an average firing rate by convolving the spike trains with a Gaussian of 10 ms SD from which we derived the root mean square difference between outputs for different sound levels (Fig. 10D). When STP was present, a greater similarity across input levels was observed compared with STP absence.

Our model predicts that particularly STP of the endbulb synapses underlies the hypothesized VNLL function of reducing spectral splatter (Spencer et al., 2015) by allowing to precisely transmit broadband information of sound transients during ongoing stimulation. STP further suppresses ongoing components of input firing; hence, the VNLL, being an inhibitory nucleus, protects this information from being suppressed in higher-order midbrain processing stages. The model also shows that, particularly for low input frequencies, as they occur especially in octopus cells during processing of natural sounds, STP widens the dynamic range of the input–output function, which confirms our experimentally derived conclusions from Figure 8. We evaluated our model by using human speech sounds, since peripheral models (cochlea and octopus cells) are currently not available for gerbil-like parameters. The mix of harmonic complexes and transients, however, is common to most natural sounds and conspecific communication; thus, we expect the same principles to apply also to a "gerbil" model. Conversely, owing to the high evolutionary conservation of mammalian auditory brainstem anatomy and the large diversity of communication sounds, we may hypothesize that auditory processing was the driver for developing communication sounds rather than having become adopted to them.

Discussion

Here we quantified the synaptic current components mediated by large somatic endbulbs onto mature VNLL neurons, and by use of dynamic-clamp recordings, their influence on supra-threshold output generation. We found that synaptic glutamate currents were composed of a slow NMDAR, and a fast, biexponentially decaying AMPAR-mediated component. The slow AMPAR current component did not contribute to output generation under physiological conditions. The STP at these endbulb synapses was composed of frequency-dependent initial facilitation followed by depression. During high-frequency activation, the NMDAR current showed a build-up, which led to a minor amplification of the supra-threshold output. When simulated synaptic inputs were randomized, the supra-threshold output generation depended on the input frequency and intensity. The latency of action potential generation was determined by the EPSG size. Mechanistically, STP generated a temporal filter supporting onset responsiveness at frequencies up to 200 Hz. Modeling suggests that this filtering restricts VNLL activity to onset responsiveness of sound transients.

The pharmacological profile of glutamate currents indicated AMPAR- and NMDAR-mediated signaling and the lack of kainate-receptor currents. Somatic calyx or endbulb synapses, as in the MNTB and the AVCN, are known for their large AMPAR-mediated EPSC with rapid decay kinetics. These AMPAR currents are supposed to be mainly based GluR4 AMPAR currents (Geiger et al., 1995; Koike-Tani et al., 2005; Lujan et al., 2019). Such currents are characterized by a strong rectification similar to the one observed here and described for VNLL neurons before (Kladisios et al., 2020). Moreover, the described biexponential AMPAR current decay has been observed in other synapses as well (Silver et al., 1996; Wall et al., 2002; Berger et al., 2014). Similar to cerebellar synapses (Wall et al., 2002), the second component of AMPAR currents at mature VNLL end bulbs is between 5% and 10% of the overall amplitude. In calyx and endbulb synapses, the presence of synaptic NMDAR currents was described in some reports (Pliss et al., 2009; Steinert et al., 2010), but not in others (Kladisios et al., 2020). Here, at ~P22, VNLL endbulbs exhibited a minor NMDAR component that slightly affected output generation. We could not detect kainate-receptor currents, similar to other adult auditory brainstem synapses (Couchman et al., 2012). Thus, previously reported presence of kainate-receptor currents in the LSO (Vitten et al., 2004) is likely restricted to juvenile animals. Glutamate currents in VNLL endbulb synapses have been studied before in mice, where they appear larger but with comparable decay kinetics (Caspari et al., 2015; Baumann and Koch, 2017). In mice, short-term depression has been shown to be the only form of plasticity, at least under 2 mM external Ca^{2+} concentration. In our recordings, the observed initial facilitation and lower depression state might be attributed to the lower external Ca^{2+} concentration of 1.2 mM. Together, endbulbs in the VNLL behave overall similar to other large somatic synapses, despite reported differences in calcium current activation in juvenile postnatal ages (Berger et al., 2014).

Short trains of afferent fiber stimulation of various frequencies are often used to determine the synaptic components and plasticity and their influence on output generation in the auditory system (e.g., Yang and Xu-Friedman, 2009; Porres et al., 2011; Nerlich et al., 2014; Baumann and Koch, 2017). Here we used dynamic clamp-based conductance train stimulations to disentangle the effect of the synaptic NMDAR and AMPAR current time course on output generation. The simulated synaptic NMDAR current build-up during ongoing high-frequency trains
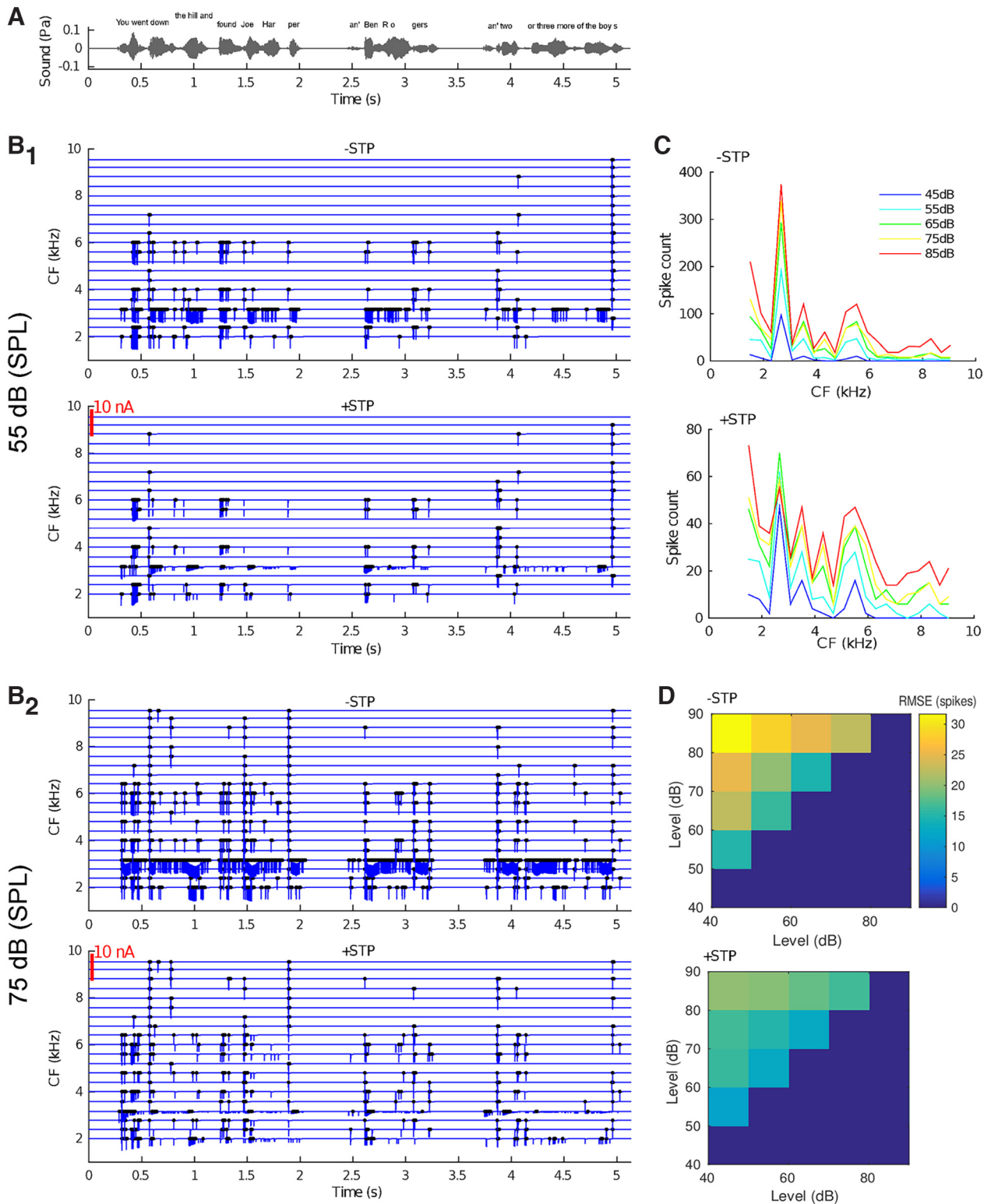
Figure 10. Model predictions of VNLL spiking on speech stimulation. *A*, Example sound stimulus (male voice at 55 dB SPL) taken from a free audiobook (https://librivox.org/the-adventures-of-huckleberry-finn-version-5-dramatic-reading-by-mark-twain/). *B*, Synaptic currents (blue; scale bar in red) and spiking (black) of VNLL neurons receiving a single synaptic input from a model octopus cell with center frequencies (CF) as indicated. Simulations are performed without (−) and with (+) STP for sound levels for 45-85 dB. *B₁*, *B₂*, Results from sound levels 55 and 75 dB, respectively. *C*, Total spike counts as a function of frequency channel and intensity level (colors) without (top) and with (bottom) STP. *D*, Mean difference (RMSE; see color bar) between firing rates (as a function of time) over all frequency channels without (top) and with (bottom) STP.

was capable to support action potential firing in the VNLL. This effect was largest at the end of the stimulation train. This NMDAR-mediated amplification was limited to ongoing high-frequency trains, did not occur in paired-pulse protocols, and

was reduced during random stimulations. Large endbulbs in the VNLL might, however, match other large synapses more closely, as in MNTB and AVCN, where NMDAR-mediated output modification has been documented (Steinert et al., 2008, 2010; Pliss et

al., 2009; but see Kladisios et al., 2020). Nevertheless, the NMDAR-dependent electrogenic output amplification seems weak in the VNLL compared with other lateral lemniscal neurons (e.g., in the DNLL) (Kelly and Kidd, 2000; Porres et al., 2011; Ammer et al., 2012; Siveke et al., 2018, 2019). The physiological size of the slow AMPAR current decay was not sufficient to alter action potential generation in ongoing EPSGs. Yet, increasing the slow simAMPA component showed that in principle a change in AMPAR kinetics is capable of altering output. This is consistent with previous work that shows that stimulation shape strongly effects action potential generation (Cathala et al., 2003; Couchman et al., 2010; Ammer et al., 2012; Lehnert et al., 2014; Franzen et al., 2015; Cao and Oertel, 2017; Kladisios et al., 2020; Bondy et al., 2021).

Neuronal activity in the auditory system is characterized by spontaneous activity (Bajo et al., 1998; Hermann et al., 2007; Kopp-Scheinpflug et al., 2008) and by sound evoked transient increases in frequency and temporal precision (Joris et al., 1994). The short stimulation trains of equally spaced time intervals do not meet these physiological characteristics, while Poisson-distributed stimulation trains are closer to the neuronal activity in the auditory system. Therefore, we consider our long Poisson-distributed stimulation trains as a good approximation for physiological conditions. These trains include relevant synaptic dynamics of adaptations and recovery period. The voltage response to these trains showed a large contribution of simSTP and a minor contribution of simNMDAR conductance to action potential generation. The effect of simNMDAR conductance was smaller compared with short train stimulations, likely because the simNMDAR current build-up is more limited because of longer, interspersed time intervals.

During neuronal processing, STP exerts functions, such as the sharpening of temporal integration (Kuba et al., 2002; Cook et al., 2003), filter functions (Fortune and Rose, 2001; Chung et al., 2002), or gain control (Rothman et al., 2009; Pedroarena, 2020). The estimated STP in the VNLL during short stimulation trains led to a strong low pass filter for output generation. This filter function was also detected during long-lasting simulated physiological stimulations. Moreover, during these physiological matching stimulations, we found that simSTP increases the dynamic range of the input–output function and therefore affects the gain of these synapses. Thus, STP can simultaneously lead to multiple effects. Concerning the simSTP-mediated filter functions, simNMDAR conductance led to a slight leftward shift. This shift can be interpreted as an increase in sensitivity for input–output functions at these endbulb synapses. In addition to gain and filter functions, our computational model indicates an additional effect of STP. STP increases the invariance to sound intensity for onset responsiveness. Thus, it allows the onset response to sound transients to be selectively fed forward irrespectively of sound intensity, while other ongoing activity is suppressed. This function combines the notion of a rapid inhibitory onset response mediated by the VNLL (for review, see Pollak et al., 2011) with the invariance of temporal precision to sound intensities (Covey and Casseday, 1991; Zhang and Kelly, 2006b; Recio-Spinoso and Joris, 2014).

We report that neuronal latency is largely a function of conductance. Neither interstimulus interval itself, the history dependence, nor simNMDAR conductance significantly altered the action potential latency. The conductance mediated latency and therefore its simSTP dependence is in agreement with the increase in jitter observed during short stimulation trains in VNLL neurons of mice (Baumann and Koch, 2017). Moreover,

this finding is consistent with the described latency dependence on neuronal leak (Franzen et al., 2015), since more leak (i.e., more conductance) reduces jitter. The conductance dependence of latency, however, appears to contradict the approximate independence of the first spike latency to sound intensity. Yet, the latency range for different conductances measured here *in vitro* is ~0.6 ms and therefore below or similar to the latency differences observed with changes in sound intensity *in vivo* (Covey and Casseday, 1991; Zhang and Kelly, 2006b; Liu et al., 2014; Recio-Spinoso and Joris, 2014).

Our data add to the understanding of the mechanistic basis of the phenotypic function of endbulb synapses. VNLL neurons are supposed to be faithfully locked with temporal fidelity to sound transients of up to 250 Hz (Zhang and Kelly, 2006a,b; Recio-Spinoso and Joris, 2014). Our data suggest that STP composed of depression and facilitation supports this faithful and precise output. NMDAR contributions thereby slightly increase the sensitivity for action potential generation. The limitation of output generation to <250 Hz stimulation also allows this synapse to be more temporally precise because, at higher input frequencies, the STD induced reduction of conductance transmits information with larger delay and imprecision. Thus, rapid and selective VNLL-induced onset inhibition in the IC achieves a sustained precision within its boundaries.

References

Adams JC (1997) Projections from octopus cells of the posteroventral cochlear nucleus to the ventral nucleus of the lateral lemniscus in cat and human. Audit Neurosci 3:335–350.

Ammer JJ, Grothe B, Felmy F (2012) Late postnatal development of intrinsic and synaptic properties promotes fast and precise signaling in the dorsal nucleus of the lateral lemniscus. J Neurophysiol 107:1172–1185.

Ammer JJ, Siveke I, Felmy F (2015) Activity-dependent transmission and integration control the timescales of auditory processing at an inhibitory synapse. Curr Biol 25:1562–1572.

Bajo VM, Villa AE, de Ribaupierre F, Rouiller EM (1998) Discharge properties of single neurons in the dorsal nucleus of the lateral lemniscus of the rat. Brain Res Bull 47:595–610.

Barry PH (1994) JPCalc, a software package for calculating liquid junction potential corrections in patch-clamp, intracellular, epithelial and bilayer measurements and for correcting junction potential measurements. J Neurosci Methods 51:107–116.

Bartos M, et al. (2002) Fast synaptic inhibition promotes synchronized gamma oscillations in hippocampal interneuron networks. Proc Natl Acad Sci USA 99:13222–13227.

Baumann VJ, Koch U (2017) Perinatal nicotine exposure impairs the maturation of glutamatergic inputs in the auditory brainstem. J Physiol 595:3573–3590.

Beiderbeck B, et al. (2018) Precisely timed inhibition facilitates action potential firing for spatial coding in the auditory brainstem. Nat Commun 9:1771.

Berger C, Meyer EM, Ammer JJ, Felmy F (2014) Large somatic synapses on neurons in the ventral lateral lemniscus work in pairs. J Neurosci 34:3237–3246.

Bondy BJ, Haimes DB, Golding NL (2021) Physiological diversity influences detection of stimulus envelope and fine structure in neurons of the medial superior olive. J Neurosci 41:6234–6245.

Borst JG (2010) The low synaptic release probability in vivo. Trends Neurosci 33:259–266.

Cao XJ, Oertel D (2017) Genetic perturbations suggest a role of the resting potential in regulating the expression of the ion channels of the KCNA and HCN families in octopus cells of the ventral cochlear nucleus. Hear Res 345:57–68.

Caspari F, Baumann VJ, Garcia-Pino E, Koch U (2015) Heterogeneity of intrinsic and synaptic properties of neurons in the ventral and dorsal parts of the ventral nucleus of the lateral lemniscus. Front Neural Circuits 9:74.

Cathala L, Brickley S, Cull-Candy S, Farrant M (2003) Maturation of EPSCs and intrinsic membrane properties enhances precision at a cerebellar synapse. J Neurosci 23:6074–6085.

Chung S, Li X, Nelson SB (2002) Short-term depression at thalamocortical synapses contributes to rapid adaptation of cortical sensory responses in vivo. Neuron 34:437–446.

Cook DL, Schwindt PC, Grande LA, Spain WJ (2003) Synaptic depression in the localization of sound. Nature 421:66–70.

Couchman K, Grothe B, Felmy F (2010) Medial superior olivary neurons receive surprisingly few excitatory and inhibitory inputs with balanced strength and short-term dynamics. J Neurosci 30:17111–17121.

Couchman K, Grothe B, Felmy F (2012) Functional localization of neurotransmitter receptors and synaptic inputs to mature neurons of the medial superior olive. J Neurophysiol 107:1186–1198.

Covey E, Casseday JH (1991) The monaural nuclei of the lateral lemniscus in an echolocating bat: parallel pathways for analyzing temporal features of sound. J Neurosci 11:3456–3470.

Cruikshank SJ, Urabe H, Nurmikko AV, Connors BW (2010) Pathway-specific feedforward circuits between thalamus and neocortex revealed by selective optical stimulation of axons. Neuron 65:230–245.

Fischer L, Leibold C, Felmy F (2018) Resonance properties in auditory brainstem neurons. Front Cell Neurosci 12:8.

Fortune ES, Rose GJ (2001) Short-term synaptic plasticity as a temporal filter. Trends Neurosci 24:381–385.

Franken TP, et al. (2021) Glycinergic axonal inhibition subserves acute spatial sensitivity to sudden increases in sound intensity. Elife 10:e62183.

Franzen DL, Gleiss SA, Berger C, Kumpfbeck FS, Ammer JJ, Felmy F (2015) Development and modulation of intrinsic membrane properties control the temporal precision of auditory brain stem neurons. J Neurophysiol 113:524–536.

Franzen DL, Gleiss SA, Kellner CJ, Kladisios N, Felmy F (2020) Activity-dependent calcium signaling in neurons of the medial superior olive during late postnatal development. J Neurosci 40:1689–1700.

Friauf E, Fischer AU, Fuhr MF (2015) Synaptic plasticity in the auditory system: a review. Cell Tissue Res 361:177–213.

Friauf E, Ostwald J (1988) Divergent projections of physiologically characterized rat ventral cochlear nucleus neurons as shown by intra-axonal injection of horseradish peroxidase. Exp Brain Res 73:263–284.

Geiger JR, et al. (1995) Relative abundance of subunit mRNAs determines gating and Ca^{2+} permeability of AMPA receptors in principal neurons and interneurons in rat CNS. Neuron 15:193–204.

Gundlfinger A, Leibold C, Gebert K, Moisel M, Schmitz D, Kempter R (2007) Differential modulation of short-term synaptic dynamics by long-term potentiation at mouse hippocampal mossy fibre synapses. J Physiol 585:853–865.

Hanson JE, Jaeger D (2002) Short-term plasticity shapes the response to simulated normal and parkinsonian input patterns in the globus pallidus. J Neurosci 22:5164–5172.

Hermann J, Pecka M, von Gersdorff H, Grothe B, Klug A (2007) Synaptic transmission at the calyx of Held under in vivo like activity levels. J Neurophysiol 98:807–820.

Hermann J, Grothe B, Klug A (2009) Modeling short-term synaptic plasticity at the calyx of Held using in vivo-like stimulation patterns. J Neurophysiol 101:20–30.

Joris PX, Carney LH, Smith PH, Yin TC (1994) Enhancement of neural synchronization in the anteroventral cochlear nucleus: I. Responses to tones at the characteristic frequency. J Neurophysiol 71:1022–1036.

Kelly JB, Kidd SA (2000) NMDA and AMPA receptors in the dorsal nucleus of the lateral lemniscus shape binaural responses in rat inferior colliculus. J Neurophysiol 83:1403–1414.

Kelly JB, van Adel BA, Ito M (2009) Anatomical projections of the nuclei of the lateral lemniscus in the albino rat (*Rattus norvegicus*). J Comp Neurol 512:573–593.

Kladisios N, Fischer L, Felmy F (2020) Minimal number of required inputs for temporally precise action potential generation in auditory brainstem nuclei. Front Cell Neurosci 14:592213.

Koike-Tani M, Saitoh N, Takahashi T (2005) Mechanisms underlying developmental speeding in AMPA-EPSC decay time at the calyx of Held. J Neurosci 25:199–207.

Kopp-Scheinpflug C, Tolnai S, Malmierca MS, Rubsamen R (2008) The medial nucleus of the trapezoid body: comparative physiology. Neuroscience 154:160–170.

Kuba H, Koyano K, Ohmori H (2002) Synaptic depression improves coincidence detection in the nucleus laminaris in brainstem slices of the chick embryo. Eur J Neurosci 15:984–990.

Kuenzel T, Borst JG, van der Heijden M (2011) Factors controlling the input–output relationship of spherical bushy cells in the gerbil cochlear nucleus. J Neurosci 31:4260–4273.

Lehnert S, et al. (2014) Action potential generation in an anatomically constrained model of medial superior olive axons. J Neurosci 34:5370–5384.

Liu HH, Huang CF, Wang X (2014) Acoustic signal characteristic detection by neurons in ventral nucleus of the lateral lemniscus in mice. Dongwuxue Yanjiu 35:500–509.

Lorteije JA, Rusu SI, Kushmerick C, Borst JG (2009) Reliability and precision of the mouse calyx of Held synapse. J Neurosci 29:13770–13784.

Lujan B, Dagostin A, von Gersdorff H (2019) Presynaptic diversity revealed by Ca(2+)-permeable AMPA receptors at the calyx of Held synapse. J Neurosci 39:2981–2994.

Markram H, Tsodyks M (1996) Redistribution of synaptic efficacy between neocortical pyramidal neurons. Nature 382:807–810.

Moore LA, Trussell LO (2017) Corelease of inhibitory neurotransmitters in the mouse auditory midbrain. J Neurosci 37:9453–9464.

Myoga MH, Lehnert S, Leibold C, Felmy F, Grothe B (2014) Glycinergic inhibition tunes coincidence detection in the auditory brainstem. Nat Commun 5:3790.

Nerlich J, Kuenzel T, Keine C, Korenic A, Rubsamen R, Milenkovic I (2014) Dynamic fidelity control to the central auditory system: synergistic glycine/GABAergic inhibition in the cochlear nucleus. J Neurosci 34:11604–11620.

Oertel D, Bal R, Gardner SM, Smith PH, Joris PX (2000) Detection of synchrony in the activity of auditory nerve fibers by octopus cells of the mammalian cochlear nucleus. Proc Natl Acad Sci USA 97:11773–11779.

Pecka M, Brand A, Behrend O, Grothe B (2008) Interaural time difference processing in the mammalian medial superior olive: the role of glycinergic inhibition. J Neurosci 28:6914–6925.

Pedroarena CM (2020) A slow short-term depression at Purkinje to deep cerebellar nuclear neuron synapses supports gain-control and linear encoding over second-long time windows. J Neurosci 40:5937–5953.

Pliss L, Yang H, Xu-Friedman MA (2009) Context-dependent effects of NMDA receptors on precise timing information at the endbulb of Held in the cochlear nucleus. J Neurophysiol 102:2627–2637.

Pollak GD, Gittelman JX, Li N, Xie R (2011) Inhibitory projections from the ventral nucleus of the lateral lemniscus and superior paraolivary nucleus create directional selectivity of frequency modulations in the inferior colliculus: a comparison of bats with other mammals. Hear Res 273:134–144.

Porres CP, Meyer EM, Grothe B, Felmy F (2011) NMDA currents modulate the synaptic input–output functions of neurons in the dorsal nucleus of the lateral lemniscus in Mongolian gerbils. J Neurosci 31:4511–4523.

Rebhan M, Leibold C (2021) A phenomenological spiking model for octopus cells in the posterior-ventral cochlear nucleus. Biol Cybern 115:331–341.

Recio-Spinoso A, Joris PX (2014) Temporal properties of responses to sound in the ventral nucleus of the lateral lemniscus. J Neurophysiol 111:817–835.

Rhode WS, Smith PH (1986) Physiological studies on neurons in the dorsal cochlear nucleus of cat. J Neurophysiol 56:287–307.

Rothman JS, Cathala L, Steuber V, Silver RA (2009) Synaptic depression enables neuronal gain control. Nature 457:1015–1018.

Saint Marie RL, Shneiderman A, Stanforth DA (1997) Patterns of gamma-aminobutyric acid and glycine immunoreactivities reflect structural and functional differences of the cat lateral lemniscal nuclei. J Comp Neurol 389:264–276.

Schofield BR, Cant NB (1997) Ventral nucleus of the lateral lemniscus in guinea pigs: cytoarchitecture and inputs from the cochlear nucleus. J Comp Neurol 379:363–385.

Sen K, Jorge-Rivera JC, Marder E, Abbott LF (1996) Decoding synapses. J Neurosci 16:6307–6318.

Silver RA, Colquhoun D, Cull-Candy SG, Edmonds B (1996) Deactivation and desensitization of non-NMDA receptors in patches and the time course of EPSCs in rat cerebellar granule cells. J Physiol 493:167–173.

Siveke I, Ammer JJ, Gleiss SA, Grothe B, Leibold C, Felmy F (2018) Electrogenic N-methyl-D-aspartate receptor signaling enhances binaural responses in the adult brainstem. Eur J Neurosci 47:858–865.

Siveke I, Lingner A, Ammer JJ, Gleiss SA, Grothe B, Felmy F (2019) A temporal filter for binaural hearing is dynamically adjusted by sound pressure level. Front Neural Circuits 13:8.

Smith PH, Massie A, Joris PX (2005) Acoustic stria: anatomy of physiologically characterized cells and their axonal projection patterns. J Comp Neurol 482:349–371.

Spencer MJ, et al. (2015) Broadband onset inhibition can suppress spectral splatter in the auditory brainstem. PLoS One 10:e0126500.

Steinert JR, et al. (2008) Nitric oxide is a volume transmitter regulating postsynaptic excitability at a glutamatergic synapse. Neuron 60:642–656.

Steinert JR, Postlethwaite M, Jordan MD, Chernova T, Robinson SW, Forsythe ID (2010) NMDAR-mediated EPSCs are maintained and accelerate in time course during maturation of mouse and rat auditory brainstem in vitro. J Physiol 588:447–463.

Stotler WA (1953) An experimental study of the cells and connections of the superior olivary complex of the cat. J Comp Neurol 98:401–431.

Vitten H, Reusch M, Friauf E, Lohrke S (2004) Expression of functional kainate and AMPA receptors in developing lateral superior olive neurons of the rat. J Neurobiol 59:272–288.

Wall MJ, Robert A, Howe JR, Usowicz MM (2002) The speeding of EPSC kinetics during maturation of a central synapse. Eur J Neurosci 15:785–797.

Wu SH (1999) Physiological properties of neurons in the ventral nucleus of the lateral lemniscus of the rat: intrinsic membrane properties and synaptic responses. J Neurophysiol 81:2862–2874.

Yang H, Xu-Friedman MA (2009) Impact of synaptic depression on spike timing at the endbulb of Held. J Neurophysiol 102:1699–1710.

Yang Y, Adowski T, Ramamurthy B, Neef A, Xu-Friedman MA (2015) High-speed dynamic-clamp interface. J Neuropysiol 113:2713–2720.

Zhang H, Kelly JB (2006a) Responses of neurons in the rat's ventral nucleus of the lateral lemniscus to amplitude-modulated tones. J Neurophysiol 96:2905–2914.

Zhang H, Kelly JB (2006b) Responses of neurons in the rat's ventral nucleus of the lateral lemniscus to monaural and binaural tone bursts. J Neurophysiol 95:2501–2512.

Zilany MS, Bruce IC, Carney LH (2014) Updated parameters and expanded simulation options for a model of the auditory periphery. J Acoust Soc Am 135:283–286.

Zilany MS, Bruce IC, Nelson PC, Carney LH (2009) A phenomenological model of the synapse between the inner hair cell and auditory nerve: long-term adaptation with power-law dynamics. J Acoust Soc Am 126:2390–2412.